ELSEVIER

Journal of Fluids and Structures 19 (2004) 681–712

JOURNAL OF
FLUIDS AND
STRUCTURES

www.elsevier.nl/locate/jnlabr/yjfls

Aeroelastic analysis of hypersonic vehicles

P.P. Friedmann[a,*], J.J. McNamara[a], B.J. Thuruthimattam[a], I. Nydick[b]

[a] University of Michigan, Ann Arbor, MI 48109-2140, USA
[b] Matsushita Electric Company of America, New Jersey, USA

Received 20 October 2003; accepted 3 April 2004

Abstract

This paper presents a fundamental study of the aeroelastic behavior of hypersonic vehicles. Two separate configurations are examined. First, a typical cross-section analysis of a double-wedge airfoil in hypersonic flow is performed using three different types of unsteady airloads: piston theory and complete Euler and Navier–Stokes solutions based on computational fluid dynamics. The analysis of the double-wedge airfoil is used to justify the usage of the simple aerodynamics for a reusable launch vehicle (RLV). Subsequently, the aeroelastic problem for a complete vehicle that resembles an RLV in trimmed flight is considered, using approximate first-order piston theory aerodynamics. The results provided for these configurations provide guidelines for approximate aeroelastic modelling of hypersonic vehicles.

1. Introduction and problem statement

Hypersonic aeroelasticity and aerothermoelasticity received considerable attention in the late 1950s and during the 1960s as evident from Bisplinghoff and Dugundji (1958), Garrick (1963), Hedgepeth and Widmayer (1963) and Laidlaw and Wyker (1963) using various versions of piston theory, as well as other very approximate aerodynamic models. This research activity was quite useful and it provided some basis for the aerothermoelastic design of the space shuttle. For a considerable time, since that early period, there was only limited interest in this area until the advent of the National Aerospace Plane (NASP) which motived new research in this field. In recent years, renewed activity in hypersonic flight research has been stimulated by the need for a low-cost, single-stage-to-orbit (SSTO) or two-stage-to-orbit (TSTO) reusable launch vehicle (RLV) and the long-term design goal of incorporating air breathing propulsion devices in this class of vehicles. The X-33, an example of the former vehicle type, was a $\frac{1}{2}$ scale, fully functional technology demonstrator for the full-scale VentureStar. Another ongoing hypersonic vehicle research program is the NASA Hyper-X experimental vehicle effort. Other activities are focused on the design of unmanned hypersonic vehicles that meet the needs of the US Air Force. The present study is aimed at enhancing the fundamental understanding of the aeroelastic behavior of vehicles that belong to this category and operate in a typical hypersonic flight envelope.

Vehicles in this category are based on a lifting body design. However, stringent minimum-weight requirements imply a degree of fuselage flexibility. Aerodynamic surfaces, needed for control, are also flexible. Furthermore, to meet the requirement of a flight profile that spans the Mach number range from 0 to 15, the vehicle must withstand severe aerodynamic heating. These factors combine to produce unusual aeroelastic problems that have received only limited attention in the past. Furthermore, it is important to emphasize that testing of aeroelastically scaled wind tunnel

---

*Corresponding author.
E-mail address: peretzf@umich.edu (P.P. Friedmann).

0889-9746/$ - see front matter © 2004 Elsevier Ltd. All rights reserved.
doi:10.1016/j.jfluidstructs.2004.04.003

Nomenclature

A	area
$\mathbf{A}$	flutter boundary eigenproblem matrix
a	nondimensional offset between the elastic axis and the midchord, positive for elastic axis behind midchord
a_∞	free-stream sound velocity
b	semi-chord of the airfoil
$\mathbf{C}(\Theta)$	orthogonal rotation matrix from the inertial axes to the body axes
C_p	pressure coefficient
C_{ft}, C_{fr}	chord length of fin tip and root, respectively
c	reference length, chord length of double-wedge airfoil
D	domain of integration of the flexible body
$\mathbf{D}(\Theta)$	transformation matrix relating the time derivatives of the Euler angles to the angular velocity vector
d_f	distance from vehicle, c.g., to leading edge of canted fin root chord
d_e	distance from vehicle, c.g., to aerodynamic center of elevon
e_T	thrust eccentricity
$\mathbf{F}$	nonconservative force vector, expressed in body axes
$\hat{\mathbf{F}}$	vector of distributed generalized forces
$f(x)$	function describing airfoil surface
g	acceleration of gravity
h	airfoil vertical displacement at elastic axis
h^b	depth distribution of equivalent plate trapezoidal segment
$\mathbf{I}$	identity matrix
I_α	mass moment of inertia about the elastic axis
$\mathbf{J}$	matrix of mass moments of inertia of the deformed body
$\mathbf{J}^\circ$	matrix of mass moments of inertia of the undeformed body
$J^0_{xx}, J^0_{yy}, J^0_{zz}, J^0_{xy}$	mass moments of inertia of the undeformed body
$\hat{J}^0_{yy}$	nondimensionalized mass moment of inertia for the undeformed hypersonic vehicle, $2J^\circ_{yy}/(p_\infty A_t l^3_{lb})$
$\mathbf{K}$	stiffness matrix
K_α, K_h	spring constants in pitch and plunge, respectively; $K_\alpha = I_\alpha \omega^2_\alpha, K_h = m\omega^2_h$
$\mathscr{L}$	matrix of structural operators on $\mathbf{u}$
L	Lagrangian of the hybrid system, written as a function of the generalized coordinates
$\tilde{L}$	Lagrangian of the hybrid system, written as a function of quasi-coordinates
$\tilde{\mathrm{L}}$	trim lift
L'	lift per unit span
L'_1, L'_2, L'_3	first-, second- and third-order piston theory lift components
l	length
M	moment component in the y-direction of the body axes
Mc	Mach number at which flutter occurs
$\mathbf{M}$	moment vector written in terms of components along the body axes
M_{EA}	moment per unit span about the elastic axis
M_1, M_2, M_3	first-, second- and third-order piston theory moment components
$\mathbf{M}^\mathbf{g}$	generalized mass matrix
M_∞	free-stream Mach number
m	mass of the flexible body
$\hat{m}$	nondimensionalized mass of the hypersonic vehicle, $2m/(\rho_\infty A_t l_{lb})$
$\bar{m}$	mass per unit area
N_m	number of normal modes in truncated series
$\hat{\mathbf{n}}$	unit normal
O	origin of the body axes
P	arbitrary point on flexible body
p, q, r	angular velocity components referred to body axes, in x-, y- and z-directions, respectively
r_α	radius of gyration
p_l	pressure on lower surface

p_s	pressure on surface
p_u	pressure on upper surface
p_∞	free-stream pressure
$\mathbf{Q}$	vector of discrete generalized forces
$\hat{\mathbf{Q}}$	vector of generalized forces used in modal expansion method
$\mathbf{q}$	vector of generalized coordinates
q_∞	free-stream dynamic pressure
$\hat{q}$	nondimensionalized pitch rate, $l_{lb}q/V_{0z}$
$\mathbf{q_x}, \mathbf{q_y}, \mathbf{q_z}, \mathbf{q_{\Phi z}}, \mathbf{q_{\Phi y}}$	vectors of the unknown power series coefficients for $u_{x0}, u_{y0}, u_{z0}, \Phi_x, \Phi_y$, respectively
$\mathbf{R}_0$	position vector of origin of body axes with respect to the inertial axes
$\mathbf{R}_0^{\mathbf{I}}$	$\mathbf{R}_0$, but with components given with respect to unit vectors of the inertial axes
$\mathbf{r}$	position vector of typical point P in the undeformed configuration with respect to the body axes
$\mathbf{r}_p$	position vector of typical point P in the deformed body with respect to the inertial axes
S_α	static mass moment of wing section about elastic axis
s_f	span of canted fin
T	kinetic energy
t	time
t_k	thickness distribution of kth layer of equivalent plate trapezoidal segment cover skin
$\hat{t}$	nondimensional time, $V_{0z}t/l_{lb}$
U	strain energy
U_0	strain energy density
U_∞, V	free-stream velocity
$\mathbf{u}$	vector of elastic displacements
$\mathbf{u}_0$	vector of elastic displacements of the reference surface
V_g	potential energy due to gravity
V_0	velocity of origin of body axes, in body axis components
v	time derivative of $\mathbf{u}$ with respect to a reference frame attached to the body axes
v_p	effective piston velocity
$\mathbf{v}_p$	velocity vector of typical point P in the deformed body with respect to the inertial axes
X, Z	components of F in the x- and y-directions of the body axes, respectively
X_I, Y_I, Z_I	inertial axes
x, y, z	body axes
x_α	nondimensional offset between the elastic axis and center of gravity, positive for center of gravity behind elastic axis
Δx	vector of degrees of freedom for linearized model of the generic hypersonic vehicle
$\bar{Z}^{u,l}(x,y)$	initial curvature of vehicle upper (u) or lower (l) surface
$Z'(x,y,t)$	position of airfoil surface
Z_c	camber distribution of equivalent plate trapezoidal segment

Greek symbols

α	angle of attack
α_s	static angle of attack
γ	specific heat
γ_c	climb angle
$\delta(\,)$	variational symbol
δ_{ij}	Kronecker delta function
δ_e	elevon deflection
$\Delta(\,)$	perturbed quantity
ε_T	inclination of the thrust vector
ζ_k	modal damping of the kth mode
η	spanwise local coordinate of equivalent plate trapezoidal segment
$\hat{\eta}_i$	nondimensionalized modal coordinate, η_i $(i = 1, \ldots, N_m), \eta_i/l_{lb}$
$\hat{\eta}N_{m+i}$	nondimensionalized modal coordinate, ηN_{m+i} $(i = 1, \ldots, N_m), \eta_i/V_{0x}$
η	vector of generalized coordinates used in modal expansion

Θ	3×1 matrix of Euler angles
θ_f	angle of the X-33 fins, measured from horizontal
ξ	streamwise local coordinate of equivalent plate trapezoidal segment
ρ	vehicle density
τ	thickness ratio of the airfoil
ϕ, θ, ψ	Euler angles, elements of Θ
$\phi_{\mathbf{x}}, \phi_{\mathbf{y}}, \phi_{\mathbf{z}}, \phi_{\Phi_z}\phi_{\Phi_y}$	vectors of power series terms for the approximating polynomials of $u_{x0}, u_{y0}, u_{z0}, \Phi_x, \Phi_y$, respectively
Φ_k	kth normal mode
Φ	modal matrix
Φ_x, Φ_y	rotations due to transverse shear in the xz and yz planes, respectively
ω	angular velocity
ω_k	natural frequency of kth normal mode
$\hat{\omega}_k$	nondimensionalized natural frequency

Special symbols

$\dot{()}$	derivative with respect to time
$()'$	derivative with respect to spatial coordinate
$\hat{()}$	indicates energy density of variable or nondimensionalized quantity, depending on context
$\tilde{()}$	skew symmetric matrix
$\bar{()}$	trimmed value
$()_{lb}$	quantity with respect to the lifting body only
$()_f$	quantity with respect to the canted fins only
$()_e$	quantity with respect to the elevon only
$()_t$	quantity with respect to the total vehicle

models, a conventional practice in subsonic and supersonic flow, is not feasible in the hypersonic regime. Thus, the role of aeroelastic simulations is more important for this flight regime than in any other flight regime.

Previous studies in this area can be separated into several groups. The first group consists of studies focusing on panel flutter, which is a localized aeroelastic problem representing a small portion of the skin on the surface of the hypersonic vehicle. Hypersonic panel flutter has been studied by a number of researchers, focusing on important effects such as aerodynamic heating (Xue and Mei, 1990), composite (Gray and Mei, 1992; Abbas and Ibrahim, 1993) and nonlinear structural models (Bein et al., 1993) and initial panel curvature (Nydick et al., 1995). It was noted in Nydick et al. (1995) that piston theory may not be appropriate for the hypersonic regime and that hypersonic studies might have to use unsteady aerodynamic loads based on the solution of the Navier–Stokes equations. A comprehensive review of this research can be found in a recent survey paper (Mei et al., 1999).

The second group of studies in this area was motivated by a previous hypersonic vehicle, namely, the NASP (Rricketts et al., 1993; Spain et al., 1993a, b; Scott and Pototzky, 1993; Rodgers, 1992; Heeg et al., 1993; Heeg and Gilbert, 1993). However, some of these studies dealt with the transonic regime, because it was perceived to be quite important. Spain et al. (1993a) carried out a flutter analysis of all-movable NASP-like wings with slab and double-wedge airfoils. They found that using effective shapes for the airfoils obtained by adding the boundary layer displacement thickness to the airfoil thickness improved the overall agreement with experiments. Aerothermoelastic analyses of NASP-like vehicles found that aerodynamic heating altered the aeroelastic stability of the vehicle through the degradation of material properties and introduction of thermal stresses (Rodgers, 1992; Heeg et al., 1993; Heeg and Gilbert, 1993).

The third group of studies is restricted to recent papers that deal with the newer hypersonic configurations such as the X-33 or the X-34. Blades et al. (1999) considered the X-34 launch vehicle in free flight at $M_\infty = 8.0$. The aeroelastic instability of a generic hypersonic vehicle, resembling the X-33, was considered in (Nydick and Friedmann, 1999) and (Nydick, 2000). It was found that at high hypersonic speeds and high altitudes, the hypersonic vehicle is stable, when first-order piston theory was used to represent the aerodynamic loads. Sensitivity of the flutter boundaries to vehicle flexibility and trim state were also considered (Nydick and Friedmann, 1999). In another reference (Gupta et al., 2001), CFD-based flutter analysis was used for the aeroelastic analysis of the X-43 configuration, using system identification-based order reduction of the aerodynamic degrees of freedom. Both the structure and the fluid were discretized using

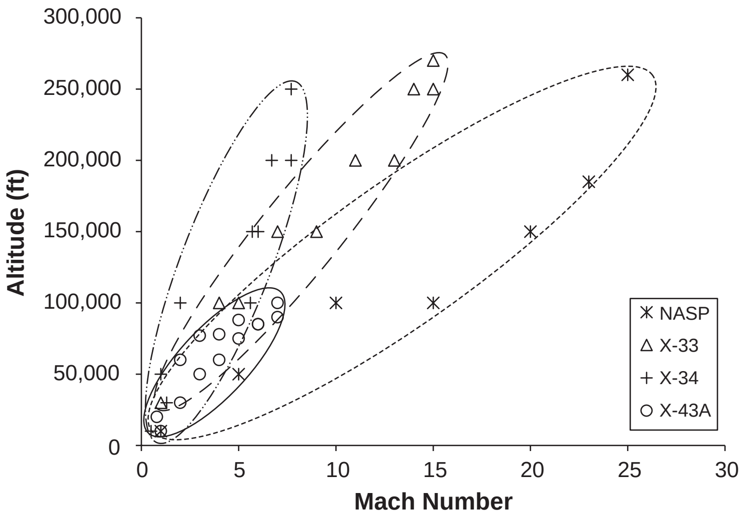

Fig. 1. Operating envelopes for several modern hypersonic vehicles.

the finite element approach. It was shown that piston theory and ARMA Euler calculations predicted somewhat similar results.

From the studies on various hypersonic vehicles (Ricketts et al., 1993; Berry et al., 1999; Riley and Alter, 1998; Gupta et al., 2001) one can identify operating envelopes for each vehicle. A graphical representation of these operating conditions is shown in Fig. 1.

In a recent study (Thuruthimattam et al., 2002), the two-dimensional aeroelastic stability problem of a double-wedge typical section in hypersonic flow has been studied. Three different unsteady types of aerodynamic loads were used in an attempt to establish the differences in stability boundaries when using: (a) piston theory; (b) computational fluid dynamics (CFD)-based Euler loads; and (c) loads based on the CFD solution of the Navier–Stokes equations. This simple model has proved itself very useful for understanding the level of approximations needed when generating unsteady aerodynamic loads. This paper has several objectives: (i) to present an aeroelastic analysis for a typical cross-section of a double-wedge airfoil in hypersonic flow and use it to compare aeroelastic stability boundaries based on unsteady aerodynamic loads obtained from piston theory, as well as loads based on CFD obtained from the Euler and Navier–Stokes equations; (ii) to present the unrestrained aeroelastic equations of motion for a generic trimmed hypersonic vehicle; and (iii) to conduct a parametric study of the aeroelastic behavior of a hypersonic vehicle in free flight and determine its aeroelastic stability characteristics.

It is important to note that this is an exploratory paper that aims to identify the value of approximate aeroelastic models in the hypersonic flow region where only a limited amount of research has been done to date.

2. Aeroelastic analysis of the double-wedge typical section in hypersonic flow

The computational aeroelastic solutions for the double-wedge typical section are obtained using the CFL3D code (Krist and Rumsey, 1997). The CFL3D code is used to perform both steady and unsteady flow calculations, and to also obtain the aeroelastic transients. The aeroelastic solution utilizes the free vibration modes of the structure.

2.1. Euler/Navier–Stokes solver in CFL3D

The aeroelastic analysis of the double-wedge airfoil is carried out using the CFL3D code. The code uses an implicit, finite-volume algorithm based on upwind-biased spatial differencing to solve the time-dependent Euler- and Reynolds-averaged Navier–Stokes equations. Multigrid and mesh sequencing are available for convergence acceleration. The algorithm, which is based on a cell-centered scheme, uses upwind differencing based on either flux-vector splitting or flux-difference splitting, and can sharply capture shock waves. For applications utilizing the thin-layer Navier–Stokes equations, different turbulence models are available. For time-accurate problems using a deforming mesh, an additional term accounting for the change in cell volume is included in the time discretization of the governing equations. Since

CFL3D is an implicit code using approximate factorization, linearization and factorization errors are introduced at every time step. Hence, intermediate calculations referred to as "subiterations" are used to reduce these errors. Increasing these subiterations improves the accuracy of the simulation, albeit at increased computational cost.

2.2. Aeroelastic option in CFL3D

The aeroelastic approach underlying the CFL3D code is similar to that described in Robinson and Yang (1991) and Cunningham and Bennett (1989). The equations are derived by assuming that the general motion $w(x, y, t)$ of the structure is described by a finite modal series given by Eq. (1) below. The functions $\phi_i(x, y)$ represent the free vibration modes of the vehicle which are calculated using a finite element approach

$$\mathbf{u}(x, y, t) = \sum_{i=1}^{N_m} q_i(t)\mathbf{\Phi}_i(x, y). \tag{1}$$

The aeroelastic equations of motion are obtained from Lagrange's equations

$$\frac{\mathrm{d}}{\mathrm{d}t}\left(\frac{\partial T}{\partial \dot{\mathbf{q}}}\right) - \frac{\partial T}{\partial \mathbf{q}} + \frac{\partial U}{\partial \mathbf{q}} = \mathbf{Q}, \tag{2}$$

which yield

$$\mathbf{M}^g \ddot{q} + \mathbf{K}q = \mathbf{Q}(\mathbf{q}, \dot{\mathbf{q}}, \ddot{\mathbf{q}}), \tag{3}$$

where the elements of the generalized force vector are given by

$$Q_i = q_\infty c^2 \int_A \mathbf{\Phi}_i \frac{p_s \mathrm{d}A}{q_\infty c^2}. \tag{4}$$

The aeroelastic equations are written in terms of a linear state-space equation (using a state vector of the form $[\ldots\ \dot{q}_{i-1}\ q_i\ \dot{q}_i\ q_{i+1}\ \ldots]^{\mathrm{T}}$) such that a modified state-transition-matrix integrator can be used to march the coupled fluid–structural system forward in time. The fluid forces are coupled with the structural equations of motion through the generalized aerodynamic forces. Thus, a time history of the modal displacements, modal velocities and generalized forces is obtained.

2.3. General overview of the solution process

The solution of the computational aeroelasticity problem used in the present study is shown in Fig. 2. First, the vehicle geometry is created using CAD software, and from this geometry a mesh generator is used to create a structured mesh for the flow domain around the body. In parallel, an unstructured mesh is created for the finite element model of the structure using the same nodes on the vehicle surface that were used to generate the fluid mesh. Subsequently, the fluid mesh is used to compute the flow around the rigid body using a CFD solver, which consists of the CFL3D code developed by NASA Langley Research Center. The structural mesh is used to obtain the free vibration modes of the structure by finite element analysis using MSC NASTRAN. Nodes on the surface of the geometry in both the structured and unstructured meshes are matched up by their physical coordinates. This correlation is used to obtain the modal displacements at each of the surface nodes in the structured fluid mesh from the unstructured structural mesh. Using the flow solution as an initial condition, and the modal information, an aeroelastic steady state is obtained. For a geometry with vertical symmetry at zero angle of attack, such as the double-wedge airfoil, the aeroelastic steady state is the same as the undeflected state. Next, the structure is perturbed in one or more of its modes by an initial modal velocity condition, and the transient response of the structure is obtained. To determine the flutter conditions at a given altitude, aeroelastic transients are computed at several Mach numbers and the corresponding dynamic pressures. The frequency and damping characteristics of the transient response for a given flight condition and vehicle configuration can be determined from the moving block approach, which analyzes the Fourier transform of a discretely sampled transient signal (Bousman and Winkler, 1981). This approach applied to the same altitude and vehicle configuration for a range of Mach numbers results in a series of damping values for the system. The flutter Mach number can be estimated from this series by interpolating the damping data-points to identify zero damping.

2.4. Computational model for the double-wedge airfoil

The Euler and Navier–Stokes computations are carried out using a 225 × 65 C-grid with 225 points around the wing and its wake (145 points wrapped around the airfoil itself), and 65 points extending radially outward from the airfoil

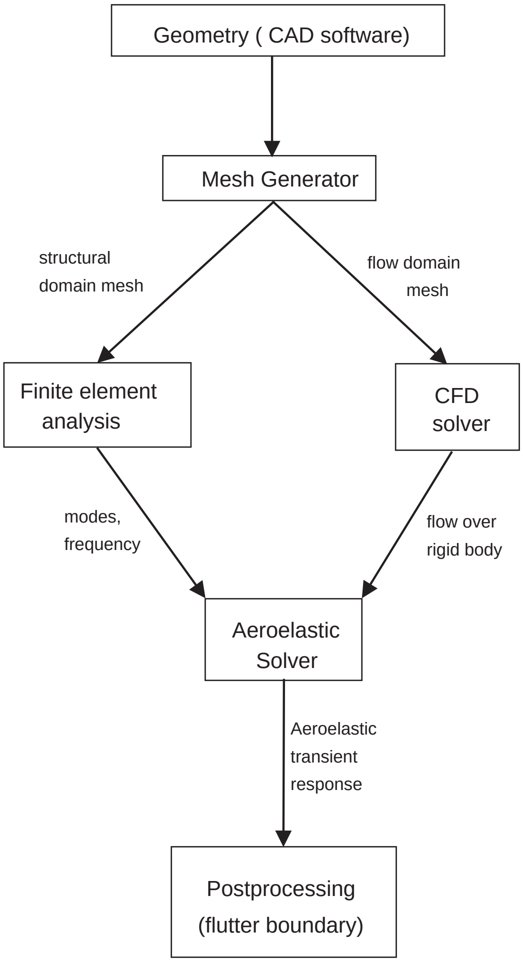

Fig. 2. A flow diagram of the computational aeroelastic solution procedure.

surface. The computational domain extends one chord-length upstream and six chord lengths downstream, and one chord length to the upper and lower boundaries. For the Navier–Stokes simulations, the Spalart–Allmaras turbulence model was used, along with an adiabatic wall temperature condition. The double-wedge airfoil and a portion of the surrounding computational grid are shown in Fig. 3.

2.5. Aeroelastic model for a double-wedge airfoil using higher-order piston theory

Piston theory is an inviscid unsteady aerodynamic theory that has been used extensively in supersonic and hypersonic aeroelasticity. It provides a point–function relationship between the local pressure on the surface of the vehicle and the component of fluid velocity normal to the moving surface (Ashley and Zartarian, 1956; Lighthill, 1953). The derivation utilizes the isentropic "simple wave" expression for the pressure on the surface of a moving piston

$$\frac{p_s(x,t)}{p_\infty} = \left(1 + \frac{\gamma - 1}{2}\frac{v_p}{a_\infty}\right)^{2\gamma/(\gamma-1)}, \tag{5}$$

where

$$v_p = \frac{\partial Z'(x,t)}{\partial t} + U_\infty \frac{\partial Z'(x,t)}{\partial x}. \tag{6}$$

The expression for piston theory is based on a binomial expansion of Eq. (5), where the order of the expansion is determined by the ratio of v_p/a_∞. Lighthill (1953) suggested a third-order expansion, since it produced the smallest

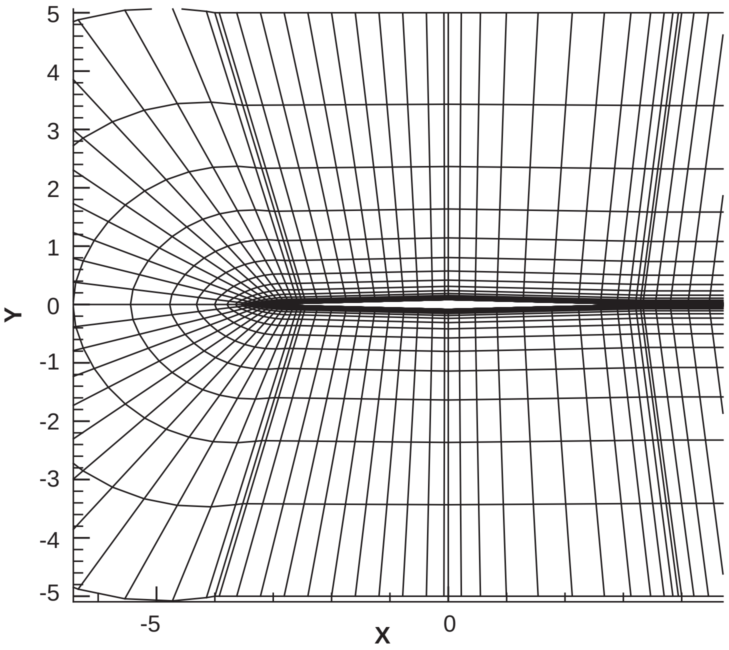

Fig. 3. Double-wedge airfoil section, and surrounding grid, to scale.

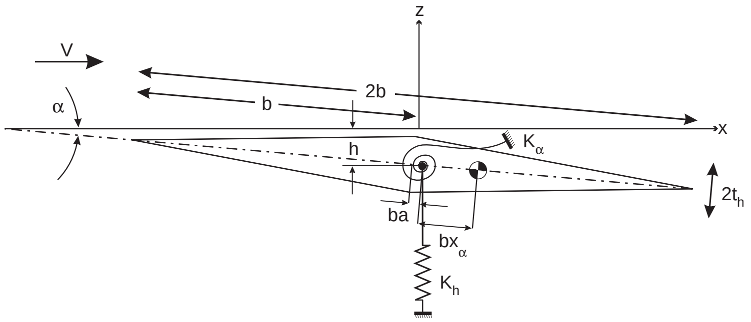

Fig. 4. Two degree of freedom typical airfoil geometry.

error of the various orders of expansion used when compared to the limiting values of pressure, namely, the ‘‘simple wave’’ and ‘‘shock expansion’’ solutions. The third-order expansion of Eq. (5) yields

$$p_s(x,t) - p_\infty = p_\infty\left[\gamma\frac{v_p}{a_\infty} + \frac{\gamma(\gamma+1)}{4}\left(\frac{v_p}{a_\infty}\right)^2 + \frac{\gamma(\gamma+1)}{12}\left(\frac{v_p}{a_\infty}\right)^3\right]. \tag{7}$$

An aeroelastic analysis for a typical cross-section for a double-wedge airfoil was developed using Eq. (7) for the unsteady pressure loading. The equations of motion for a typical cross-section, with pitch and plunge degrees of freedom shown in Fig. 4, were obtained from Lagrange's equations

$$\begin{aligned} &m\ddot{h} + S_\alpha\ddot{\alpha} + K_h h = -L'(t),\\ &S_\alpha\ddot{h} + I_\alpha\ddot{\alpha} + K_\alpha\alpha = M_{EA}(t). \end{aligned} \tag{8}$$

Assuming small displacements and using Fig. 4 yields

$$Z'(x,t) = -\{h(t) + (x - ba)\alpha(t)\} + f(x) \tag{9}$$

and

$$\begin{aligned} v_{pu} &= -\{\dot{h} + (x - ba)\dot{\alpha}\} + U_\infty\left\{-\alpha + \frac{\partial f(x)}{\partial x}\right\}, \\ v_{pl} &= \{\dot{h} + (x - ba)\dot{\alpha}\} - U_\infty\left\{-\alpha + \frac{\partial f(x)}{\partial x}\right\}, \end{aligned} \tag{10}$$

where

$$\begin{aligned} &\frac{\partial f_u(x)}{\partial x} = \tau\colon\ -b<x<0, \\ &\frac{\partial f_u(x)}{\partial x} = -\tau\colon\ 0<x<b, \\ &\frac{\partial f_l(x)}{\partial x} = -\tau\colon\ -b<x<0, \\ &\frac{\partial f_l(x)}{\partial x} = \tau\colon\ 0<x<b. \end{aligned} \tag{11}$$

From Eqs. (7), (10) and (11) the unsteady pressure distribution was determined. The unsteady lift and moment due to this pressure distribution were determined from

$$\begin{aligned} L'(t) &= \int_{-b}^{b} (p_l(x,t) - p_u(x,t))\,\mathrm{d}x, \\ M_{EA}(t) &= -\int_{-b}^{b} (x - ba)\,(p_l(x,t) - p_u(x,t))\,\mathrm{d}x. \end{aligned} \tag{12}$$

The unsteady lift can be written as

$$L'(t) = L'_1(t) + L'_2(t) + L'_3(t), \tag{13}$$

where

$$\begin{aligned} L'_1(t) &= 4p_\infty\gamma M_\infty b\left\{\frac{\dot{h}}{V} - ba\frac{\dot{\alpha}}{V} + \alpha\right\}, \\ L'_2(t) &= -p_\infty\gamma(\gamma+1)M_\infty^2 b^2\tau\left(\frac{\dot{\alpha}}{V}\right), \\ L'_3(t) &= \frac{1}{3}p_\infty\gamma(\gamma+1)M_\infty^3 b\left\{\left(\frac{\dot{h}}{V} - ba\frac{\dot{\alpha}}{V} + \alpha\right)\left(\left(\frac{\dot{h}}{V} - ba\frac{\dot{\alpha}}{V} + \alpha\right)^2 + 3\tau^2 + \left(b\frac{\dot{\alpha}}{V}\right)^2\right)\right\}. \end{aligned} \tag{14}$$

Note that $L_1(t)$, $L_2(t)$, and $L_3(t)$ represent the first-, second- and third-order piston theory lift components, respectively. The unsteady moment is represented in a similar manner

$$M_{EA}(t) = M_1(t) + M_2(t) + M_3(t), \tag{15}$$

where

$$\begin{aligned} M_1(t) &= 4p_\infty\gamma M_\infty b^2\left\{a\frac{\dot{h}}{V} - \left(\frac{b}{3} + ba^2\right)\frac{\dot{\alpha}}{V} + a\alpha\right\}, \\ M_2(t) &= p_\infty\gamma(\gamma+1)M_\infty^2 b^2\tau\left\{\frac{\dot{h}}{V} - 2ba\frac{\dot{\alpha}}{V} + \alpha\right\}, \end{aligned}$$

$$\begin{aligned} M_3(t) = -\frac{1}{3}p_\infty\gamma(\gamma+1)M_\infty^3 b^2 &\left\{\frac{1}{5}\left(b\frac{\dot{\alpha}}{V}\right)^3 - a\left(\frac{\dot{h}}{V} - ba\frac{\dot{\alpha}}{V} + \alpha\right)\left(\left(\frac{\dot{h}}{V} - ba\frac{\dot{\alpha}}{V} + \alpha\right)^2 + 3\tau^2\right)\right. \\ &\left. + b\frac{\dot{\alpha}}{V}\left(\left(\frac{\dot{h}}{V} - ba\frac{\dot{\alpha}}{V} + \alpha\right)^2 + \tau^2 - ba\frac{\dot{\alpha}}{V}\left(\frac{\dot{h}}{V} - ba\frac{\dot{\alpha}}{V} + \alpha\right)\right)\right\}. \end{aligned} \tag{16}$$

It is interesting to note that the second-order lift and moment are linear in terms of the displacement variables due to vertical symmetry of the double-wedge airfoil.

For compatibility with CFL3D, it is important to represent Eq. (8) in terms of generalized coordinates and forces. This is accomplished by the normal mode transformation given by

$$\begin{Bmatrix} h(t) \\ \alpha(t) \end{Bmatrix} = [\mathbf{\Phi}]\begin{Bmatrix} q_1(t) \\ q_2(t) \end{Bmatrix}. \tag{17}$$

Applying the normal mode transformation on the equations of motion, Eq. (8), yields

$$\begin{Bmatrix} \ddot{q}_1(t) \\ \ddot{q}_2(t) \end{Bmatrix} = [\mathbf{\Phi}]^{\mathrm{T}}\begin{Bmatrix} L(t) \\ M_{EA}(t) \end{Bmatrix} - \begin{bmatrix} \omega_1^2 & 0 \\ 0 & \omega_2^2 \end{bmatrix}\begin{Bmatrix} q_1(t) \\ q_2(t) \end{Bmatrix}, \tag{18}$$

for mass normalized modes. The modal degrees of freedom are coupled through the generalized aerodynamic loads. Eq. (18) was solved using the subroutine ODE45 in MATLAB©.

2.6. Results on the aeroelastic stability of the double-wedge typical section

The results presented in this section compare aeroelastic stability boundaries using piston theory with those based on CFD solutions of the Euler and Navier–Stokes equations. By comparing these three sets of results, one can identify the importance of viscosity and the effectiveness of piston theory in approximating the aeroelastic behavior of a double-wedge typical section in inviscid flow.

The configuration is based on the parameters given in Table 1, the material of the structure is assumed to be aluminum alloy 2024-T3. Fig. 5 depicts the flutter boundaries at various altitudes, as a function of the offset a, for the operating envelope of a typical hypersonic vehicle, at 0° angle of attack, based on first- and third-order piston theory. The mass ratios for the various altitudes, calculated using the standard-atmosphere, are given in Table 2. It is quite interesting to compare the flutter boundaries obtained with first- and third-order piston theory at altitudes of 40 000 ft and 70 000 ft. For both cases, for the high Mach number regime, there are large differences between the flutter margins predicted by the linear and nonlinear versions of piston theory. There is a large reduction in aeroelastic stability when going from first- to third-order piston theory, particularly in the high Mach number regime. This difference diminishes as the Mach number regime decreases. It is evident that for positive values of the offset a, the first-order curves tend to asymptotically approach the curves based on third-order piston theory. For the Mach number range of $\phi < M_\infty < 15$, the height selected for the flutter calculations of this configuration was 70 000 ft. At this altitude, the flutter boundaries are at $M_c = 9.21$ for $a = 0.1$ and at $M_c = 14.96$ for $a = -0.2$. Sample computational points from this study were Mach numbers 7, 10 and 15 at 70 000 ft, with Reynolds numbers of 3.336×10^6, 4.766×10^6 and 7.149×10^6, respectively.

The results for the aeroelastic behavior with $a = 0.1$ using different aerodynamic models is shown in Fig. 6. The linear nature of the second-order piston theory model allowed an eigenanalysis for comparison with frequency and damping characteristics from second-order piston theory aeroelastic transients. From this figure, the flutter Mach number predicted by second-order piston theory was $M_c = 9.79$. In general, results from the time history analysis agreed with the eigenanalysis. The sharp coalesce shown in Fig. 6 is due to an inability of the moving block approach to distinguish between the damping and frequency characteristics of the transient motion as the flutter Mach number is approached and the two modes begin to interact. The flutter Mach number obtained with Euler aerodynamics is $M_c = 6.75$, and when Navier–Stokes aerodynamics is used, flutter is found to be at $M_c = 6.59$.

For a different offset between midchord and elastic axis, $a = -0.2$, Fig. 7 indicates that differences in system response from the three aerodynamic models are minor at Mach numbers well below the flutter boundaries. However, these differences increase with Mach number. An eigenanalysis using second-order piston theory indicates flutter at $M_c = 15.16$, while an analysis of third-order piston theory aeroelastic transients indicates flutter at $M_c = 14.96$. It is apparent that, for this configuration, third-order piston theory is slightly more conservative than second-order piston theory. With Euler aerodynamics, the flutter boundary drops to $M_c = 11.76$, and using Navier–Stokes aerodynamics results in a further reduction to $M_c = 11.15$. These differences emphasize the importance of aerodynamic nonlinearities and viscosity with increasing Mach numbers.

All the cases considered were at 0° static angle of attack. Hypersonic vehicles in trimmed flight will operate at an angle of attack. The effect of static angle of attack with $a = -0.2$ is shown in Fig. 8, using Euler aerodynamics. Three static angles of attack $\alpha_s = 0°$, $\alpha_s = 1°$ and $\alpha_s = 2°$ were considered. Increasing the static angle of attack reduces the flutter margin proportionally by a small value. Results with piston theory and Navier–Stokes aerodynamics, not shown here, exhibit similar trends.

Table 1
Properties of the configuration

Parameter	Configuration I
c (m)	2.00
Thickness ratio (%)	2.5
Wedge angle (deg)	2.86
m (kg/m)	51.8
r_α	0.5
ω_h (Hz)	7.96
ω_α (Hz)	19.9
$\frac{\omega_h}{\omega_\alpha}$	0.4
x_α	0.2

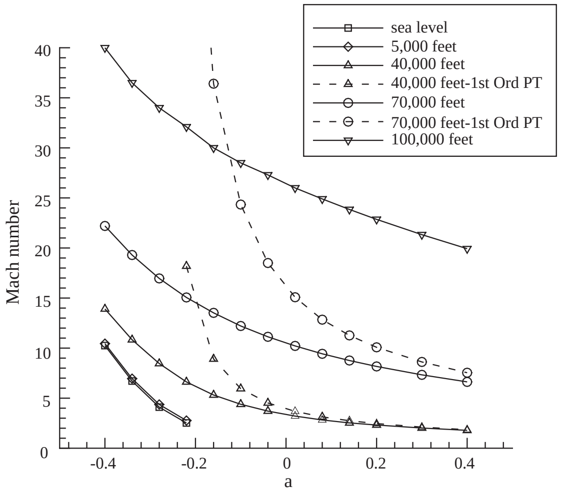

Fig. 5. Flutter boundaries at zero angle of attack, obtained using two different versions of piston theory. Full lines are for third-order piston theory, dashed lines are for first-order piston theory and the symbols on the lines identify the altitude.

Table 2
Mass ratio at various altitudes

Altitude (ft)	μ_m, Configuration I
0	13.47
5000	15.63
40 000	141.81
70 000	232.68
100 000	942.60

The results shown in this section, together with additional results shown in (Thuruthimattam et al., 2002) indicate that trend-type studies based on piston theory produce reasonable trends. The computational requirements for Euler equations are quite substantial, while Navier–Stokes solutions are very expensive. Thus when dealing with a complete hypersonic vehicle, the use of the simple piston theory, for a trend type study, can be justified based on computational cost. The problem of a complete hypersonic vehicle in trimmed flight is considered in the next section.

3. Aeroelastic analysis of a trimmed generic hypersonic vehicle

An aeroelastic analysis of the entire vehicle in free flight in the hypersonic regime requires the formulation of the governing equations of motion for an unrestrained flexible vehicle. A general discussion of the governing equations of

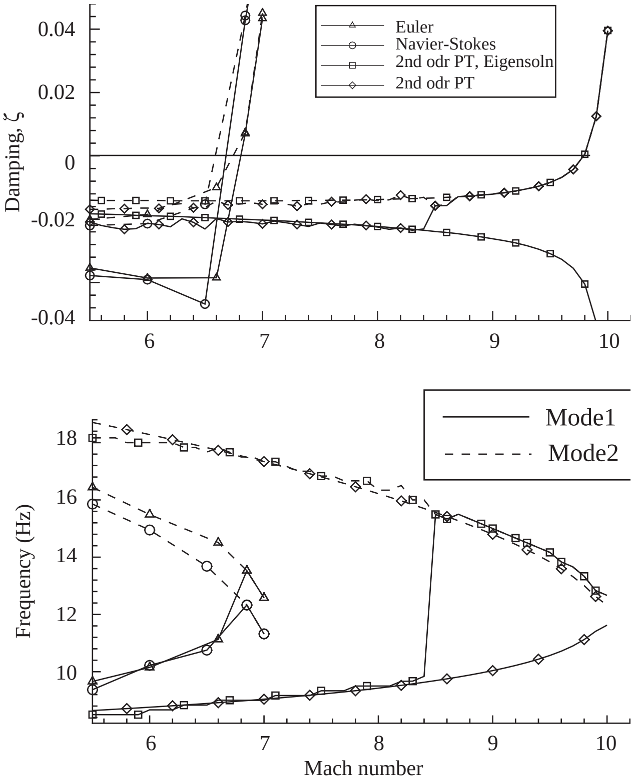

Fig. 6. Comparison of aeroelastic results at an altitude of 70 000 ft, $a = 0.1$, with different aerodynamic models.

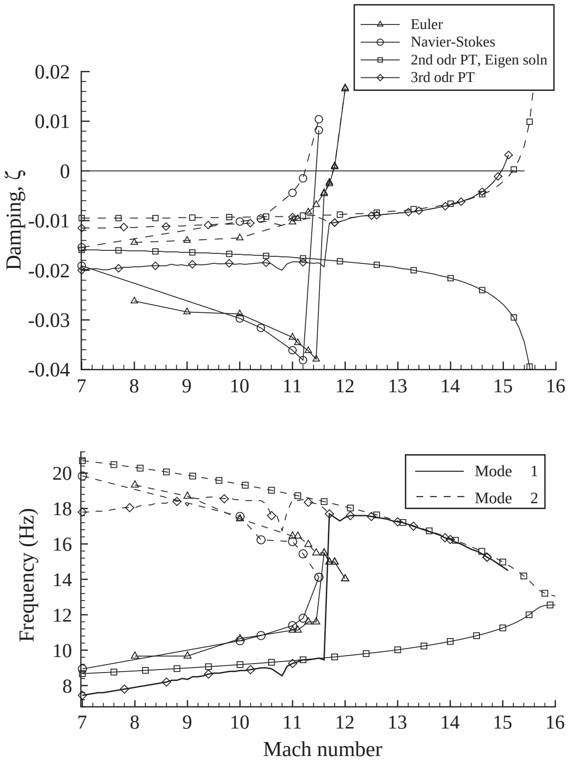

Fig. 7. Comparison of aeroelastic results at an altitude of 70 000 ft, $a = -0.2$, with different aerodynamic models.

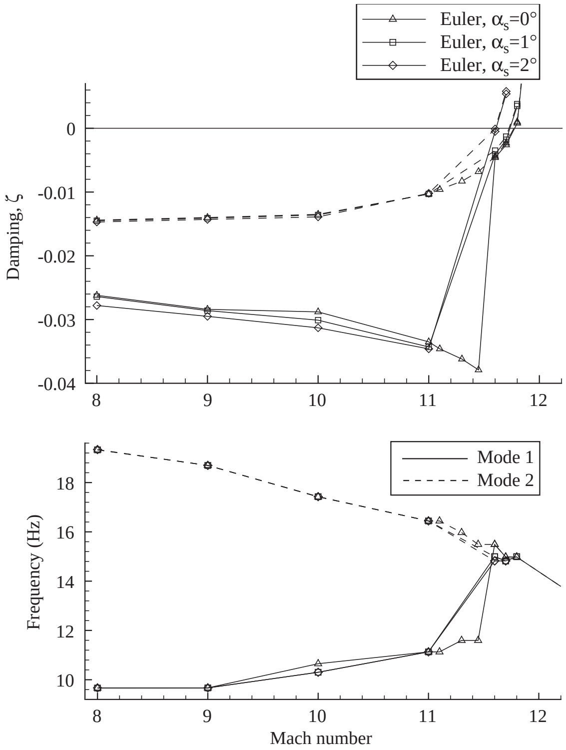

Fig. 8. Effect of static angle of attack on the aeroelastic behavior, at an altitude of 70 000 ft, using Euler aerodynamics, $a = -0.2$.

motion for unrestrained flight vehicles can be found in the text by Bisplinghoff et al. (1955) and the series of papers by Milne (1955, 1968). Application to hypersonic vehicles has been studied by Waszak and Schmidt (1988) and Bilimoria and Schmidt (1995) where the primary emphasis has been on stability and control. A novel approach to the determination of the governing equations of motion of a flexible body using quasi-coordinates has been presented by Meirovitch (1991). The method of quasi-coordinates is an effective and labor-saving procedure for obtaining the governing equations for flexible structures involving rigid body and flexible degrees of freedom.

When representing the dynamics of a flexible aerospace vehicle, several alternatives exist. One can develop a finite element model for a vehicle, which usually involves a large number of degrees of freedom. The finite element degrees of freedom can be reduced by calculating a limited number of free vibration modes and using a normal mode transformation. An alternative to the finite element method is the equivalent plate theory, which produces significant savings in both computational time and model setup effort while retaining acceptable modelling accuracy (Giles, 1986). Recently, equivalent plate theory has received renewed attention and its modelling capabilities have been expanded so that it is now capable of representing complex aerospace vehicle structural configurations (Giles, 1989, 1995; Livne, 1993). Such enhancements include the ability to model asymmetric fin cross-sections, out-of-plane fin segments, internal web and spar structures, including transverse shear effects, thermal stresses and general boundary conditions, as well as the ability to specify multiple trapezoidal segments and multiple sets of assumed displacement functions. In this study, equivalent plate theory is employed to calculate the free vibration modes of the unrestrained vehicle using the ELAPS code.

3.1. Equations of motion of the unrestrained vehicle

The derivation of the equations of motion for the unrestrained generic hypersonic vehicle is based upon Lagrange's equations of motion in terms of quasi-coordinates following the approach described in Meirovitch (1991).

Quasi-coordinates are defined in terms of their time derivatives. Specifically, these time derivatives are defined as nonintegrable linear combinations of the generalized velocities. Because the time derivatives are nonintegrable, the quasi-coordinate itself is undefined.

The coordinate systems needed to describe the translating and rotating elastic body are shown in Figs. 9 and 10. The body axes translate and rotate with the body, though they are not necessarily attached to a specific material point in the body. Possible choices for the body axes include attached axes, mean axes and principal axes (Milne, 1955). Attached axes are attached to a specific material point in the body, mean axes are oriented such that no linear or angular momentum is generated by the flexible motion, and principal axes are oriented such that they are the principal axes of the deforming body at all times. Mean axes are used in this study.

As shown in Meirovitch (1991) and Nydick and Friedmann (1999), after considerable algebraic manipulation, Lagrange's equations may be rewritten in terms of time

$$\frac{\mathrm{d}}{\mathrm{d}t}\left(\frac{\partial \bar{L}}{\partial \mathbf{V}_0}\right) + \tilde{\boldsymbol{\omega}}\frac{\partial \bar{L}}{\partial \mathbf{V}_0} - \mathbf{C}\frac{\partial \bar{L}}{\partial \mathbf{R}_0^{\mathbf{I}}} = \mathbf{F}, \tag{19a}$$

$$\frac{\mathrm{d}}{\mathrm{d}t}\left(\frac{\partial \bar{L}}{\partial \omega}\right) + \tilde{\mathbf{V}}_0\frac{\partial \bar{L}}{\partial \mathbf{V}_0} + \tilde{\boldsymbol{\omega}}\frac{\partial \bar{L}}{\partial \boldsymbol{\omega}} - (\mathbf{D}^{\mathrm{T}})^{-1}\frac{\partial \bar{L}}{\partial \boldsymbol{\Theta}} = \mathbf{M}, \tag{19b}$$

$$\frac{\mathrm{d}}{\mathrm{d}t}\left(\frac{\partial \hat{T}}{\partial \mathbf{v}}\right) - \frac{\partial \hat{T}}{\partial \mathbf{u}} + \frac{\partial \hat{V}^*}{\partial \mathbf{u}} + \mathscr{L}\mathbf{u} = \hat{\mathbf{F}}, \tag{19c}$$

where $\mathbf{F}$ and $\mathbf{M}$ are nonconservative force and torque vectors, respectively, written in terms of components along the body axes and the displacements $\mathbf{u}$ are subject to appropriate boundary conditions. The bar above the Lagrangian indicates that it is to be expressed in terms of time derivatives of quasi-coordinates.

The equations for a translating and rotating flexible body may be completed by substituting appropriate expressions for the Lagrangian. Using the geometry given in Fig. 9, the position and velocity of material point P can be written as

$$\mathbf{r}_p = \mathbf{R}_0 + \mathbf{r} + \mathbf{u}, \tag{20a}$$

$$\mathbf{v}_p = \dot{\mathbf{R}}_0 + \boldsymbol{\omega} \times (\mathbf{r} + \mathbf{u}) + \mathbf{v}, \tag{20b}$$

and expressions for the kinetic and potential energy may be obtained. When small deformations are assumed, the displacements are expressed as a sum of unrestrained normal modes

$$\mathbf{u}(\mathbf{r}, t) = \sum_{k=1}^{Nm} \boldsymbol{\Phi}_k(\mathbf{r})\eta_k(t) = \boldsymbol{\Phi}\boldsymbol{\eta}, \tag{21}$$

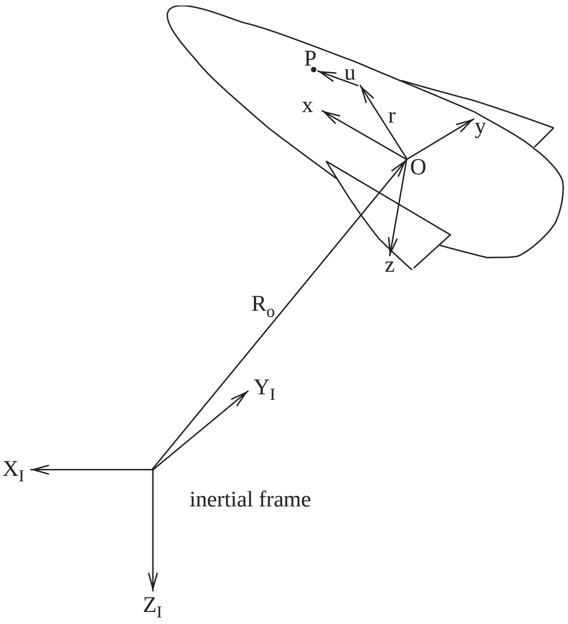

Fig. 9. Flexible body.

where the modes satisfy the orthogonality relations given by

$$\int_V \boldsymbol{\Phi}_i \cdot \boldsymbol{\Phi}_j \rho \, \mathrm{d}V = M_i^g \delta_{ij}, \tag{22}$$

where $M_i^{\mathbf{g}}$ is the ith generalized mass. This orthogonality property holds for both the rigid body and flexible modes.

Simplification of the kinetic energy expression can be obtained by employing mean axes with the origin at the center of gravity of the deformed vehicle as the body axes. Mean axes reduce the inertial coupling between the rigid and flexible equations of motion. Mean axes are chosen such that, at every instant, the linear and angular momenta of the relative motion with respect to the body axes are identically zero, which leads to the relations (Milne, 1955)

$$\int_V \rho \mathbf{u} \, \mathrm{d}V = 0, \tag{23}$$

$$\int_V \rho \mathbf{r} \times \mathbf{u} \, \mathrm{d}V = 0. \tag{24}$$

For mean axes, the kinetic energy expression becomes

$$T = \frac{1}{2} m \mathbf{V}_0^{\mathrm{T}} \mathbf{J}^0 \omega + \frac{1}{2} \int_D \rho [2\mathbf{r}^{\mathrm{T}} \tilde{\omega}^{\mathrm{T}} \tilde{\omega} \boldsymbol{\Phi} \boldsymbol{\eta} + \boldsymbol{\eta}^{\mathrm{T}} \boldsymbol{\Phi}^{\mathrm{T}} \tilde{\omega}^{\mathrm{T}} \tilde{\omega} \, \boldsymbol{\Phi} \boldsymbol{\eta}] \, \mathrm{d}D + \frac{1}{2} \dot{\boldsymbol{\eta}}^{\mathrm{T}} \mathbf{M}^g \dot{\boldsymbol{\eta}}. \tag{25}$$

The potential energy is written

$$U = \tfrac{1}{2} \boldsymbol{\eta}^{\mathrm{T}} \mathbf{K}^{\mathbf{g}} \boldsymbol{\eta} \tag{26}$$

and

$$V_g = -mgR_{0Z}^I. \tag{27}$$

The final equations of motion of the unrestrained vehicle can be written as (Nydick and Friedmann, 1999; Nydick, 2000)

$$m\dot{\mathbf{V}}_0 = m\tilde{\mathbf{V}}_0 \boldsymbol{\omega} - \mathbf{C} \frac{\partial V_g}{\partial \mathbf{R}_0^{\mathbf{I}}} + \mathbf{F}, \tag{28a}$$

$$\mathbf{J}^0 \dot{\boldsymbol{\omega}} = -\tilde{\boldsymbol{\omega}} \mathbf{J}^0 \boldsymbol{\omega} + \mathbf{M}, \tag{28b}$$

$$\mathbf{M}^{\mathbf{g}} \ddot{\boldsymbol{\eta}} + \mathbf{C}^{\mathbf{g}} \dot{\boldsymbol{\eta}} + \left(\mathbf{K}^{\mathbf{g}} - \int_D \rho \boldsymbol{\Phi}^{\mathrm{T}} \tilde{\omega}^{\mathrm{T}} \tilde{\omega} \boldsymbol{\Phi} \, \mathrm{d}D \right) \boldsymbol{\eta} = \int_D \rho \mathbf{r}^{\mathrm{T}} \tilde{\omega}^{\mathrm{T}} \tilde{\omega} \boldsymbol{\Phi} \, \mathrm{d}D + \hat{\mathbf{Q}}. \tag{28c}$$

This study focuses on the longitudinal dynamics of a symmetric vehicle in horizontal flight, which can be decoupled from the lateral equations and written as

$$m(\dot{V}_{0x} + qV_{0z}) = X - mg \sin \theta, \tag{29a}$$

$$m(\dot{V}_{0z} - qV_{0x}) = Z + mg \cos \theta, \tag{29b}$$

$$j_{yy}^0 \dot{q} = M. \tag{29c}$$

The equation governing the elastic motion remains unchanged.

3.2. Trim state of the vehicle

Aeroelastic stability boundaries are obtained from dynamic equations linearized about a static trim state; the geometry for trim is shown in Figs. 10 and 11. Lateral trim is assumed to be satisfied and decoupled from the longitudinal trim state. Longitudinal trim is obtained for level, ascending or descending flight by using elevons located at the trailing edge of the lifting body, as shown in Fig. 11(a). The trim state of the vehicle involves three primary quantities: $\bar{\alpha}, \bar{\delta}_e$, and T. These quantities are depicted in Fig. 11(a), which shows the hypersonic vehicle in climb at an angle, $\bar{\gamma}_c$, which is equal to the Euler angle, θ.

Four sets of axes are used to describe the vehicle. The first set is an inertial axis system, X_I, Y_I, Z_I, attached to a flat earth. The second set is a stability axis system, X_s, Y_s, Z_s, located at the vehicle center of gravity (c.g.) and initially aligned with the equilibrium flight velocity, $\bar{V}_0$. It is obtained from the inertial axes by locating them at the vehicle center of mass and rotating about Y_I by the angle, $\bar{\gamma}_c + \Delta\theta$, where $\Delta\theta = 0$ in the trim state. The third is a body axis system, x_b, y_b, z_b, obtained by rotating the stability axes about y_s by the trim angle of attack, $\bar{\alpha}$, which aligns the x_b axis

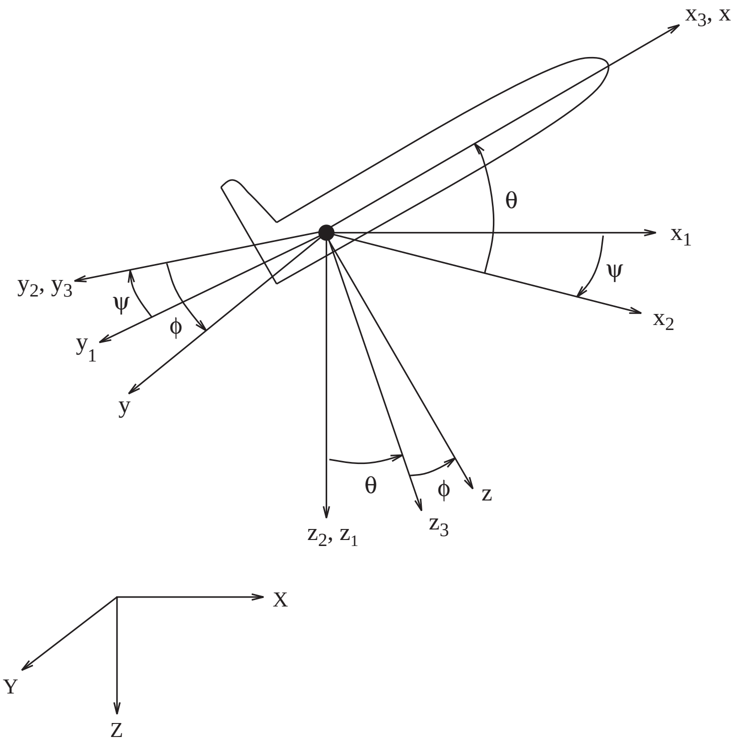

Fig. 10. Definition of Euler angles.

with the zero lift line (ZLL). The fourth system is the x_{bi}, y_{bi}, z_{bi} body axis (shown in Fig. 12), obtained from the x_b, y_b, z_b system by shifting the axes origin to the junction of the right fin trailing edge and the main lifting body and rotating about x_b by the fin inclination angle, θ_f, which directs the y_{bi}-axis outward along the right fin. This additional system is needed to represent the aerodynamic loads on the canted fin surfaces.

The net aerodynamic force acting on the vehicle is given by the lift, $\bar{L}$, and the drag, $\bar{D}$, also shown in Fig. 11(a). Alternatively, the net aerodynamic force may be resolved into components, $\bar{N}$, normal to the zero lift line and, $\bar{A}$, parallel to the zero lift line; or components, $\bar{Z}^a$ and $\bar{X}^A$, directed along the stability axes, z_s and x_s, respectively. Because the x_s-axis is initially oriented in the direction of V_0, $\bar{Z}_s^a$ equals the trim lift, $\bar{L}$, and $\bar{X}_s^a$ equals the trim drag, $\bar{D}$. However, if the vehicle is perturbed from the trim state the forces $\bar{Z}_s^a$ and $\bar{X}_s^a$ will differ from L and D, respectively.

In order to account for the effect of thrust on the trim state, a general case is considered where the thrust has an eccentricity, e_T, and can be inclined by an angle, ε_T, relative to the vehicle zero lift line. Enforcing force and moment equilibrium conditions in the vertical plane, with respect to the stability axes, yields the trim equations in nondimensional form.

$$C_{\bar{T}_R}\cos(\varepsilon_T + \bar{\alpha}) - C_{\bar{D}_R} = C_W \sin\bar{\gamma}_c, \tag{30a}$$

$$C_{\bar{T}_R}\sin(\varepsilon_T + \bar{\alpha}) + C_{\bar{L}_R} = C_W \cos\bar{\gamma}_c, \tag{30b}$$

$$C_{\bar{M}_R} + C_{\bar{T}_R} e_T = 0, \tag{30c}$$

where

$$C_{\bar{L}_R} = \frac{\bar{L}_R}{\frac{1}{2}\rho_\infty \bar{V}_{0x}^2 A_t}, \quad C_{\bar{D}_R} = \frac{\bar{D}_R}{\frac{1}{2}\rho_\infty \bar{V}_{0x}^2 A_t}, \quad C_{\bar{M}_R} = \frac{\bar{M}_R^a}{\frac{1}{2}\rho_\infty \bar{V}_{0x}^2 A_t l_{lb}},$$
$$C_{\bar{T}_R} = \frac{\bar{T}_R}{\frac{1}{2}\rho_\infty \bar{V}_{0x}^2 A_t}, \quad C_W = \frac{mg}{\frac{1}{2}\rho_\infty \bar{V}_{0x}^2 A_t}.$$

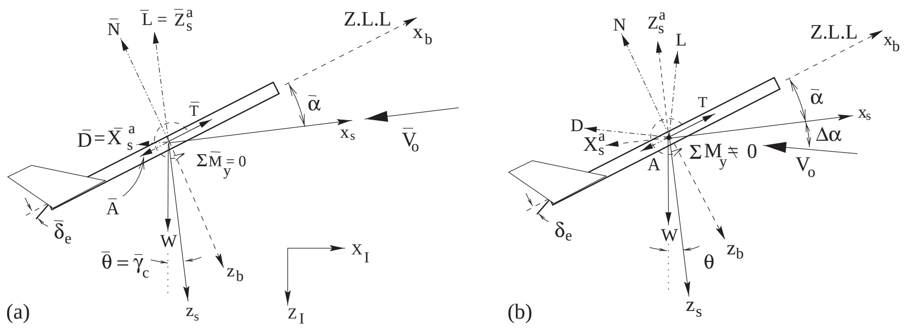

Fig. 11. Forces and moments on vehicle. (a) Trim flight condition and (b) perturbed flight condition.

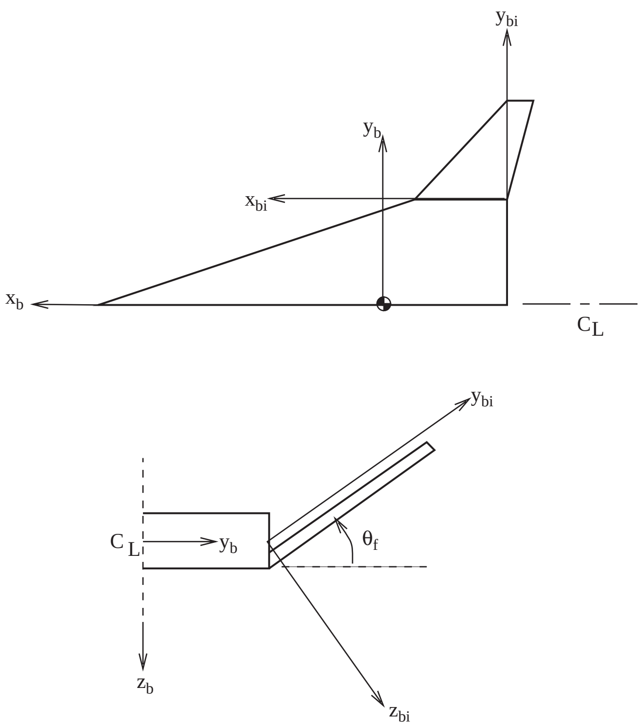

Fig. 12. Coordinate systems for X-33 main lifting body and wing.

For trim purposes, only the aerodynamic loads are steady (static) and are evaluated by treating the vehicle as a rigid plate-like structure. The aerodynamic loads are approximated using modified Newtonian theory (Lees, 1955), which states that the pressure coefficient is given by (Rasmussen, 1994)

$$C_p = \begin{cases} C_{p\max}\left(\dfrac{\bar{\mathbf{V}}_0 \cdot \hat{n}}{\bar{V}_\infty}\right)^2, & \bar{\mathbf{V}}_0 \cdot \hat{\mathbf{n}} < 0, \\ 0, & \bar{\mathbf{V}}_0 \cdot \hat{\mathbf{n}} \geqslant 0, \end{cases} \tag{31}$$

where $C_{p\max}$ is the maximum value of the pressure coefficient, evaluated at a stagnation point behind a normal shock wave, i.e.,

$$C_{p\max} = \frac{2}{\gamma M_\infty^2}\left[\left(\frac{\gamma+1}{2}M_\infty^2\right)^{\gamma/(\gamma-1)}\left(\frac{\gamma+1}{2\gamma M_\infty^2-\gamma+1}\right)^{1/(\gamma-1)} - 1\right]. \tag{32}$$

Note from Eq. (31) that the pressure is assumed to be equal to the free-stream pressure on those parts of the body for which $\bar{\mathbf{V}}_0 \cdot \hat{\mathbf{n}} \geqslant 0$. These parts of the body are said to lie in the *aerodynamic shadow*.

The lift, drag and moment are obtained by integrating the pressure over the fuselage, canted fins, and elevon separately, and summing each contribution. The resulting aerodynamic forces are given by

$$C_{\bar{L}} = C_{p\max}\left[\sin^2\bar{\alpha}\cos\bar{\alpha}\frac{A_{lb}}{A_t} + 2\sin^2\bar{\alpha}\cos\bar{\alpha}\cos^3\theta_f\frac{A_f}{A_t} + \sin^2(\bar{\alpha}+\bar{\delta}_e)\cos(\bar{\alpha}+\bar{\delta}_e)\frac{A_e}{A_t}\right], \tag{33a}$$

$$C_{\bar{D}} = C_{p\max}\left[\sin^3\bar{\alpha}\frac{A_{lb}}{A_t} + 2\sin^3\bar{\alpha}\cos^3\theta_f\frac{A_f}{A_t} + \sin^3(\bar{\alpha}+\bar{\delta}_e)\frac{A_e}{A_t}\right], \tag{33b}$$

$$\begin{aligned} C_{\bar{M}} = C_{p\max}\Bigg\{&\frac{\sin^2\bar{\alpha}}{A_t l_{lb}}\left[\frac{s_1 w_{lb}^3}{24} - \frac{1}{4}s_1 s_2 w_{lb}^2 + \frac{1}{2}(s_2^2 - d_f^2 - c_{fr}^2 - 2d_f c_{fr})w_{lb}\right] \\ &- \sin^2\bar{\alpha}\cos^3\theta_f\left[\frac{2(d_f + c_{fr} + c_{ft})}{l_{lb}}\frac{A_f}{A_t} - \frac{1}{A_t l_{lb}}\right. \\ &\left.\times\left(\frac{1}{3}(s_4^2 - s_3^2)s_f^3 + s_4 m_2 s_f^2 + m_2^2 s_f\right)\right] - \sin^2(\bar{\alpha}+\bar{\delta}_e)\cos(\bar{\alpha}+\bar{\delta}_e)\frac{d_e}{l_{lb}}\frac{A_e}{A_t}\Bigg\}, \end{aligned} \tag{33c}$$

where

$$s_1 = \frac{2(l_{lb} - c_{fr})}{w_{lb}}, \quad s_2 = l_{lb} - c_{fr} - d_f, \quad s_3 = \frac{c_{ft}}{s_f}, \quad s_4 = \frac{c_{fr}}{s_f}.$$

The trim state is calculated by solving Eqs. (30) with the aerodynamic loads given by Eqs. (33) using a nonlinear rootfinding routine.

3.3. Linearization of equations of motion

The equations of motion (Eqs. (29)) can be linearized about the steady-state trim conditions by introducing a small time-dependent perturbation, denoted by the symbol Δ in the various quantities representing forces, moments, as well as rigid body and flexible degrees of freedom.

Since the vehicle was trimmed by referencing forces and moments to the stability axes, the subscript ‘s’ has been added to these terms to indicate that they are to be interpreted as components taken along the stability axes. The various vehicle axes which were previously discussed are shown for the vehicle in perturbed flight in Fig. 11(b). Also, because a linear structural model is used for the vehicle, coupling between the steady-state deflections due to the trim forces, η_k, and the perturbed motion variables is neglected. The linear structural model is justified because generic hypersonic vehicles can be assumed to be relatively stiff, and therefore will have only small deflections due to elastic deformations.

Substitution of the expressions for the perturbed motion variables into the nonlinear longitudinal equations of motion, and subsequent elimination of all higher-order terms, results in the linearized equations

$$m\Delta\dot{v}_{0x} = -mg\cos\bar{\theta}\Delta\theta + \Delta X_s, \tag{34a}$$

$$m\Delta\dot{v}_{0z} = m\bar{V}_{0x}\Delta q - mg\sin\bar{\theta}\Delta\theta + \Delta Z_s, \tag{34b}$$

$$J_{yy}^0\Delta\dot{q} = \Delta M_s, \tag{34c}$$

$$\Delta\dot{\theta} = \Delta q, \tag{34d}$$

$$\Delta\ddot{\eta}_k + 2\xi_k\omega_k\Delta\dot{\eta}_k + \omega_k^2\Delta\eta_k = \frac{\Delta\hat{Q}_k}{M_k^g}, \quad k = 1, \ldots, N_m. \tag{34e}$$

Further simplification of the linearized equations is obtained by recognizing that coupling between the rigid body and elastic degrees of freedom will only involve the short period mode. Coupling is assumed to be negligible between the long period (phugoid) mode and the elastic degrees of freedom due to the large separation in the natural frequencies. Furthermore, the perturbation in forward speed, Δv_{0x}, has a negligible effect on the short period mode, for typical flight vehicles. Thus, $\Delta v_{0x} = 0$ and the equation governing Δv_{0x} is discarded. The rigid body equations of motion after this simplification are

$$m\Delta\dot{v}_{0z} = m\bar{V}_{0x}\Delta q + \Delta Z_s, \tag{35a}$$

$$J^0_{yy}\Delta\dot{q} = \Delta M_s. \tag{35b}$$

The force and moment perturbations, ΔZ_s and ΔM_s, are expressed in terms of partial derivatives with respect to the degrees of freedom. Eqs. (34e), (35a) and (35b) can be rewritten in terms of nondimensional flutter derivatives

$$\hat{m}D_{\hat{t}}\Delta\alpha = C_{z\alpha}\Delta\alpha + (\hat{m} + C_{zq})\Delta\hat{q} + \sum_{i=1}^{Nm}\{C_{z\eta i}\Delta\hat{\eta}_i + C_{z\dot{\eta}i}\Delta\hat{\eta}_{N_{m+i}}\} + C_{z\delta_e}\Delta\delta_e, \tag{36a}$$

$$\hat{J}^0_{yy}D_{\hat{t}}\hat{q} = C_{m\alpha}\Delta\alpha + C_{mq}\Delta\hat{q} + \sum_{i=1}^{Nm}\{C_{m\eta i}\Delta\hat{\eta}_i + C_{m\dot{\eta}i}\Delta\hat{\eta}_{N_{m+i}}\} + C_{m\delta_e}\delta_e, \tag{36b}$$

$$\begin{aligned}\hat{M}^g_k D_{\hat{t}}\hat{\eta}_{N_{m+k}} = {} & C_{Q_k\alpha}\Delta\alpha + C_{Q_k}q\Delta\hat{q} + \sum_{i=1}^{Nm}\{(C_{Q_k\eta l} - \hat{\omega}^2_k\hat{M}^g_k\delta_{kl})\Delta\hat{\eta}_l \\ & + (C_{Q_k\dot{\eta}l} - 2\xi_k\hat{\omega}_k\hat{M}^g_k\delta_{kl})\Delta\hat{\eta}_{N_{m+l}}\} + C_{Q_k\delta_e}\Delta\delta_e,\end{aligned} \tag{36c}$$

$$D_{\hat{t}}\Delta\hat{\eta}_k = \Delta\hat{\eta}_{N_{m+k}}, \quad k = 1, \ldots, N_m, \tag{36d}$$

where the various nondimensional quantities and the definitions of the flutter derivative are given in Appendix A. Additional details are also given in (Nydick and Friedmann, 1999) and (Nydick, 2000).

3.4. Calculation of the flutter derivatives

The results provided in Section 2 indicate that the general trends of aeroelastic behavior predicted when using unsteady airloads based on piston theory and the more accurate Euler equations are similar. Furthermore, often the differences between Euler-based solutions and those based on the complete Navier–Stokes equations are also fairly small. Therefore, when dealing with the aeroelastic stability of a hypersonic vehicle in high speed flight, it is reasonable to use piston theory to generate the unsteady loads when only general trends, and not the exact stability boundary, is sought. The primary advantage of this approach is the very large reduction in computational time required for the analysis of the vehicle. The purpose of this section is to obtain flutter derivatives that are suitable for a linear aeroelastic analysis and therefore linear piston theory is used for the derivation of the flutter derivatives.

The local pressure on the surface of the vehicle due to combined rigid body motion and structural deformation is

$$p_s = \rho_\infty a_\infty v_p + p_\infty, \tag{37}$$

where v_p is the velocity of a fluid particle on the surface of the vehicle in the direction normal to the surface.

The vehicle considered here has three principal types of lifting surfaces: a clipped delta-shaped lifting body, two canted fins and an elevon (see Fig. 12). The flutter derivatives of the entire vehicle are obtained by combining the individual contributions. The velocities of fluid particles on the upper and lower surfaces of the clipped delta-shaped lifting body are given by (assuming $V_{0x} \gg V_{0z}$)

$$v^u_p(x_b) = V_{0x}\cos\bar{\alpha}\left(\frac{\partial u_z}{\partial x_b} + \frac{\partial\bar{Z}^u}{\partial x_b}\right) - \dot{u}_z + x_b q - V_{0z}\cos\bar{\alpha}, \tag{38a}$$

$$v^l_p(x_b) = -V_{0x}\cos\bar{\alpha}\left(\frac{\partial u_z}{\partial x_b} + \frac{\partial\bar{Z}^l}{\partial x_b}\right) + \dot{u}_z - x_b q + V_{0z}\cos\bar{\alpha}. \tag{38b}$$

The net pressure is the sum of the trimmed pressure and the change in pressure due to the small perturbations in the rigid body and flexible degrees of freedom. This change in pressure is given by

$$\Delta p_s = \rho_\infty a_\infty \Delta v_p, \tag{39}$$

where Δv_p is the portion of v_p due to the perturbed motion

$$\Delta v^u_p(x) = \bar{V}_{0x}\cos\bar{\alpha}\frac{\partial\Delta u_z}{\partial x} - \Delta\dot{u}_z + x\Delta q - \cos\bar{\alpha}\Delta v_{0z}, \tag{40a}$$

$$\Delta v^1_p(x) = -\bar{V}_{0x}\cos\bar{\alpha}\frac{\partial u_z}{\partial x} + \Delta\dot{u}_z - x\Delta q + \cos\bar{\alpha}\Delta v_{0z}. \tag{40b}$$

Combining Eqs. (39) and (40) gives the net pressure difference between the upper and lower surfaces due to the perturbed motion

$$\Delta p_s^u - \Delta p_s^l = 2\rho_\infty a_\infty \left(\bar{V}_{0x} \cos\bar{\alpha} \frac{\partial \Delta u_z}{\partial x} - \Delta \dot{u}_z + x\Delta q - \cos\bar{\alpha}\Delta v_{0z} \right). \tag{41}$$

The aerodynamic force in the z_b-direction on the main lifting body may be written as

$$\begin{aligned} \Delta Z_{lb,b} = & \int_{A_{lb}} (\Delta p_s^u - \Delta p_s^l)\,\mathrm{d}A_{lb} \\ & = 2\rho_\infty a_\infty \bar{V}_{0z} \cos\bar{\alpha} \sum_{i=1}^{Nm} \left(\int_{A_{lb}} \frac{\partial \Phi_i^z}{\partial x_b}\,\mathrm{d}A_{lb} \Delta\eta_i \right) \\ & \quad - 2\rho_\infty a_\infty \sum_{i=1}^{Nm} \left(\int_{A_{lb}} \Phi_i^z\,\mathrm{d}A_{lb} \Delta\dot{\eta}_i \right) \\ & \quad + 2\rho_\infty a_\infty \int_{A_{lb}} x_b\,\mathrm{d}A_{lb} \Delta q - 2\rho_\infty a_\infty A_{lb} \cos\bar{\alpha}\Delta v_{0z}. \end{aligned} \tag{42}$$

The force component along the z_s-axis is given by

$$\begin{aligned} \Delta Z_{lb} & = \Delta Z_{lb,b} \cos\bar{\alpha} \\ & = \sum_{i=1}^{Nm} Z_{lb_{\eta_i}} \Delta\eta_i + \sum_{i=1}^{Nm} Z_{lb_{\dot{\eta}_i}} \Delta\dot{\eta}_i + Z_{lb_q} \Delta q + Z_{lb_{v_{0z}}} \Delta v_{0z}. \end{aligned} \tag{43}$$

The contributions of the lifting body to the Z flutter derivatives are

$$Z_{lb_{\eta_i}} = 2\rho_\infty a_\infty \bar{V}_{0x} \cos^2\bar{\alpha} \int_{A_{lb}} \frac{\partial \Phi_i^z}{\partial x}\,\mathrm{d}A_{lb}, \tag{44a}$$

$$Z_{lb_{\dot{\eta}_i}} = -2\rho_\infty a_\infty \cos\bar{\alpha} \int_{A_{lb}} \Phi_i^z\,\mathrm{d}A_{lb}, \tag{44b}$$

$$Z_{lb_q} = 2\rho_\infty a_\infty \cos\bar{\alpha} \int_{A_{lb}} x\,\mathrm{d}A_{lb}, \tag{44c}$$

$$Z_{lb_{v_{0z}}} = -2\rho_\infty a_\infty A_{lb} \cos^2\bar{\alpha}. \tag{44d}$$

The contribution of the main lifting body to the pitching moment flutter derivatives may be evaluated in a similar manner. Using Eqs. (21) and (41), the pitching moment contributed by the clipped delta-shaped lifting body may be expressed as

$$\Delta M_{lb} = -\int_{A_{lb}} (\Delta p_s^u - \Delta p_s^l) x_b\,\mathrm{d}A_{lb}. \tag{45}$$

Substitution of Eqs. (21) and (41) into Eq. (45) yields the contributions of the lifting body to the pitching moment flutter derivatives

$$M_{lb_{\eta_i}} = -2\rho_\infty a_\infty \bar{V}_{0x} \cos\bar{\alpha} \int_{A_{lb}} \frac{\partial \Phi_i^z}{\partial x_b} x_b\,\mathrm{d}A_{lb}, \tag{46a}$$

$$M_{lb_{\dot{\eta}_i}} = 2\rho_\infty a_\infty \int_{A_{lb}} \Phi_i^z x_b\,\mathrm{d}A_{lb}, \tag{46b}$$

$$M_{lb_q} = -2\rho_\infty a_\infty \int_{A_{lb}} x_b^2\,\mathrm{d}A_{lb}, \tag{46c}$$

$$M_{lb_{v_{0z}}} = 2\rho_\infty a_\infty \cos\bar{\alpha} \int_{A_{lb}} x_b\,\mathrm{d}A_{lb}. \tag{46d}$$

The final set of flutter derivatives to be calculated are those associated with the generalized forces, $\hat{Q}_i$. These forces are determined by examining the expression for the virtual work done by a virtual elastic displacement over an arbitrary surface area, A

$$\delta W = \int_A (\Delta p_s^u - \Delta p_s^l)\delta u_z \, \mathrm{d}A = \int_A (\Delta p_s^u - \Delta p_s^l)\left(\sum_{i=1}^{Nm} \Phi_i^z \delta\eta_i\right) \mathrm{d}A$$
$$= \sum_{i=1}^{Nm} \hat{Q}_i \delta\eta_i. \tag{47}$$

From Eq. (47), with $A = A_{lb}$, the contribution of the main lifting body to $\hat{Q}_i$ is

$$\hat{Q}_i^{lb} = \int_{A_{lb}} (\Delta p_s^u - \Delta p_s^l)\Phi_i^z \, \mathrm{d}A_{lb}. \tag{48}$$

Substituting Eq. (41) into Eq. (48) and expanding yields the contributions of the lifting body to the elastic generalized force derivatives

$$\hat{Q}^{lb}_{i_{\eta_j}} = 2\rho_\infty a_\infty \bar{V}_{0x} \cos\bar{\alpha} \int_{A_{lb}} \Phi_i^z \frac{\partial \Phi_j^z}{\partial x_b} \mathrm{d}A_{lb}, \tag{49a}$$

$$\hat{Q}^{lb}_{i_{\dot{\eta}_j}} = -2\rho_\infty a_\infty \int_{A_{lb}} \Phi_j^z \phi_j^z \, \mathrm{d}A_{lb}, \tag{49b}$$

$$Z_{lb_q} = 2\rho_\infty a_\infty \cos\bar{\alpha} \int_{A_{lb}} x \, \mathrm{d}A_{lb}, \tag{49c}$$

$$Z_{lb_{v_{0z}}} = -2\rho_\infty a_\infty A_{lb} \cos^2\bar{\alpha}. \tag{49d}$$

The contribution of the canted fins to the flutter derivatives is obtained in a similar manner. The velocities of fluid particles on the upper and lower surfaces of the fin due to the perturbed motion are given by

$$\Delta v_p^u(x) = \bar{V}_{0x} \cos\bar{\alpha} \frac{\partial u_{z'}}{\partial x'} - \dot{u}_{z'} + x\Delta q \cos\theta_f - \Delta v_{0z} \cos\bar{\alpha}\cos\theta_f, \tag{50a}$$

$$\Delta v_p^1(x) = -\bar{V}_{0x} \cos\bar{\alpha} \frac{\partial u_{z'}}{\partial x'} + \dot{u}_{z'} - x\Delta q \cos\theta_f + \Delta v_{0z} \cos\bar{\alpha}\cos\theta_f, \tag{50b}$$

where an additional primed coordinate system for the fin has been introduced, as shown in Fig. 12. Substitution of Eqs. (50) into Eq. (39) gives the net pressure difference between the upper and lower surfaces of the fin due to the perturbed motion

$$\Delta p_s^u - \Delta p_s^l = 2\rho_\infty a_\infty \left(\bar{V}_{0x} \cos\bar{\alpha} \frac{\partial u_{z'}}{\partial x'} - \dot{u}_{z'} + x\Delta q - \cos\theta_f - \Delta v_{0z} \cos\bar{\alpha}\cos\theta_f\right). \tag{51}$$

The net aerodynamic force in the z_s-direction on the two fins is given by

$$\Delta Z_f = 2\cos\bar{\alpha}\cos\theta_f \int_{A_f} (\Delta p_s^u - \Delta p_s^l) \, \mathrm{d}A_f, \tag{52}$$

where the contributions from each fin can be summed because both the vehicle and the motion are symmetric. Substituting Eq. (51) into Eq. (52) yields the contribution of the two canted fins to the Z flutter derivatives

$$\Delta Z_w = 4\cos\theta_f \rho_\infty a_\infty \bar{V}_{0x} \int_{A_w} \sum_{i=1}^{Nm} \mathrm{d}A_w \eta_i - 4\cos\theta_f \rho_\infty a_\infty \int_{A_w} \sum_{i=1}^{Nm} \phi_i \, \mathrm{d}A_w \dot{\eta}_i$$
$$+ \ 4\cos^2\theta_f \rho_\infty a_\infty \int_{A_w} x \, \mathrm{d}A_w \delta q - 4\cos^2\theta_f \rho_\infty a_\infty A_w \delta v_{0z}. \tag{53}$$

The contribution of the fins to the Z flutter derivatives are

$$z_{f\eta_i} = 4\cos\theta_f \cos^2\bar{\alpha} \rho_\infty a_\infty \bar{V}_{0x} \int_{A_f} \frac{\partial \phi_i^{z'}}{\partial x'} \mathrm{d}A_f, \tag{54a}$$

$$z_{f\dot{\eta}_i} = -4\cos\theta_f \cos\bar{\alpha} \rho_\infty a_\infty \int_{A_f} \phi_i^{z'} \, \mathrm{d}A_f, \tag{54b}$$

$$z_{f_q} = 4\cos^2\theta_f \cos\bar{\alpha}\rho_\infty a_\infty \int_{A_f} x\,\mathrm{d}A_f, \tag{54c}$$

$$z_{f_{v_{0z}}} = -4\cos^2\theta_f \cos^2\bar{\alpha}\rho_\infty a_\infty A_f. \tag{54d}$$

The contribution of the canted fins to the pitching moment is given by

$$\Delta M_f = -2\cos\theta_f \int_{A_f} x(\Delta p_s^u - \Delta p_s^l)\,\mathrm{d}A_f. \tag{55}$$

Since Eq. (55) differs from Eq. (52) only by the factor $\cos\bar{\alpha}$ outside the integral and the factor $-x$ inside the integral, the M_f flutter derivatives may be obtained from the Z_f flutter derivatives

$$M_{f\eta_i} = -4\cos\theta_f \cos\bar{\alpha}\rho_\infty a_\infty \bar{V}_{0x} \int_{A_f} x \frac{\partial\phi_i^{z'}}{\partial x'}\,\mathrm{d}A_f, \tag{56a}$$

$$M_{f\dot{\eta}_i} = 4\cos\theta_f \rho_\infty a_\infty \int_{A_f} x\phi_i^{z'}\,\mathrm{d}A_f, \tag{56b}$$

$$M_{f_q} = -4\cos^2\theta_f \rho_\infty a_\infty \int_{A_f} x^2\,\mathrm{d}A_f, \tag{56c}$$

$$M_{f_{v_{0z}}} = 4\cos^2\theta_f \cos\bar{\alpha}\,\rho_\infty a_\infty \int_{A_f} x\,\mathrm{d}A_f. \tag{56d}$$

Using the principle of virtual work in a manner similar to Eq. (46), the contribution of the canted fins to $\hat{Q}_i$ is given by

$$\hat{Q}_i^f = 2\int_{A_f} (\Delta p_s^u - \Delta p_s^l)\Phi_i^{z'}\,\mathrm{d}A_f. \tag{57}$$

The $\hat{Q}_i^f$ flutter derivatives may be obtained from the $\hat{Q}_i^{lb}$ flutter derivatives by referring the mode shapes to the primed (fin) coordinate system and multiplying the derivatives with respect to q and v_{0z} by $\cos\theta_f$

$$\hat{Q}_{i\eta_j}^f = 4\rho_\infty a_\infty \bar{V}_{0x}\cos\bar{\alpha} \int_{A_f} \Phi_i^{z'} \frac{\partial\Phi_j^{z'}}{\partial x'}\,\mathrm{d}A_f, \tag{58a}$$

$$\hat{Q}_{i\dot{\eta}_j}^f = -4\rho_\infty a_\infty \int_{A_f} \Phi_i^{z'}\Phi_j^{z'}\,\mathrm{d}A_f, \tag{58b}$$

$$\hat{Q}_{i_q}^f = 4\cos\theta_f \rho_\infty a_\infty \int_{A_f} \Phi_i^{z'} x\,\mathrm{d}A_f, \tag{58c}$$

$$\hat{Q}_{i_{v_{0z}}}^f = -4\cos\theta_f \rho_\infty a_\infty \cos\bar{\alpha} \int_{A_f} \Phi_i^{z'}\,\mathrm{d}A_f. \tag{58d}$$

Using the same procedure with which the flutter derivatives of the lifting body and canted fins were calculated, the contribution of the rigid elevon to the flutter derivatives is found to be

$$\Delta Z_{e_{v_{0z}}} = -2\rho_\infty a_\infty \cos^2(\bar{\alpha} + \bar{\delta}_e)\,A_e, \tag{59a}$$

$$\Delta Z_{e_{\Delta_q}} = -2\rho_\infty a_\infty \cos(\bar{\alpha} + \bar{\delta}_e)\cos\bar{\delta}_e A_e, \tag{59b}$$

$$\Delta M_{e_{v_{0z}}} = -2\rho_\infty a_\infty \cos(\bar{\alpha} + \bar{\delta}_e)\cos\bar{\delta}_e A_e, \tag{59c}$$

$$\Delta M_{e_{\Delta_q}} = -2\rho_\infty a_\infty \cos^2\bar{\delta}_e d_e^2 A_e. \tag{59d}$$

Note that since the elevon is assumed to be rigid, all of the flutter derivatives involving elastic deflection are zero. In particular, the effect of the deformation of the main lifting body on the perturbation aerodynamic forces experienced by the elevon is assumed to be negligible.

The overall flutter derivatives of the entire vehicle can be written as a combination of the individual components for which the flutter derivatives have been evaluated in the preceding parts of this section. Using Eqs. (44), (46), (49), (54), (56), (58), (59) and nondimensionalizing the derivatives using Eqs. (A.2), the flutter derivatives for the entire vehicle are given by

$$C_{z\alpha} = \frac{4\cos^2\bar{\alpha}}{M_\infty}\left\{\left(\frac{A_{lb}}{A_t}\right) + 2\frac{A_f}{A_t}\cos^2\theta_f + \left(\frac{A_e}{A_t}\right)\frac{\cos^2(\bar{\alpha}+\bar{\delta}_e)}{\cos\bar{\alpha}}\right\}, \tag{60a}$$

$$C_{zq} = \frac{4\cos\bar{\alpha}}{M_\infty A_t l_{lb}}\left(\int_{A_{lb}} x\,\mathrm{d}A_{lb} + 2\cos^2\theta_f \int_{A_f} x\,\mathrm{d}A_f - A_e d_e \cos\delta_e \frac{\cos(\bar{\alpha}+\bar{\delta}_e)}{\cos\bar{\alpha}}\right), \tag{60b}$$

$$C_{z\eta_i} = \frac{4 l_{lb}\cos^2\bar{\alpha}}{M_\infty A_t}\left(\int_{A_{lb}} \frac{\partial\phi_i^z}{\partial x}\,\mathrm{d}A_{lb} + 2\cos\theta_f \int_{A_f} \frac{\partial\phi_i^{z'}}{\partial x'}\,\mathrm{d}A_f\right), \tag{60c}$$

$$C_{z\dot{\eta}_i} = \frac{4\cos\bar{\alpha}}{M_\infty A_t}\left(\int_{A_{lb}} \phi_i^z\,\mathrm{d}A_{lb} + 2\cos\theta_f \int_{A_f} \phi_i^{z'}\,\mathrm{d}A_f\right), \tag{60d}$$

$$C_{m\alpha} = \frac{4\cos\bar{\alpha}}{M_\infty A_t l_{lb}}\left(\int_{A_{lb}} x\,\mathrm{d}A_{lb} + 2\cos^2\theta_f \int_{A_f} x\,\mathrm{d}A_f - A_e d_e \cos\delta_e \frac{\cos(\bar{\alpha}+\bar{\delta}_e)}{\cos\bar{\alpha}}\right), \tag{61a}$$

$$C_{mq} = -\frac{4}{M_\infty A_t l_{lb}^2}\left(\int_{A_{lb}} x^2\,\mathrm{d}A_{lb} + 2\cos^2\theta_f \int_{A_f} x^2\,\mathrm{d}A_f + A_e d_e \cos^2\bar{\delta}_e\right), \tag{61b}$$

$$C_{m\eta_i} = -\frac{4\cos\bar{\alpha}}{M_\infty A_t}\left(\int_{A_{lb}} \frac{\partial\phi_i^z}{\partial x} x\,\mathrm{d}A_{lb} + 2\cos\theta_f \int_{A_f} \frac{\partial\phi_i^{z'}}{\partial x'} x\,\mathrm{d}A_f\right), \tag{61c}$$

$$C_{m\dot{\eta}_i} = \frac{4}{M_\infty A_t l_{lb}}\left(\int_{A_{lb}} \phi_i^z x\,\mathrm{d}A_{lb} + 2\cos\theta_f \int_{A_f} \phi_i^z x\,\mathrm{d}A_f\right), \tag{61d}$$

$$C_{Q_k\alpha} = -\frac{4\cos\bar{\alpha}}{M_\infty A_t}\left(\int_{A_{lb}} \phi_k^z\,\mathrm{d}A_{lb} + 2\cos\theta_f \int_{A_f} \phi_k^{z'}\,\mathrm{d}A_f\right), \tag{62a}$$

$$C_{Q_k q} = \frac{4}{M_\infty A_t l_{lb}}\left(\int_{A_{lb}} \phi_k^z\, x\,\mathrm{d}A_{lb} + 2\cos\theta_f \int_{A_f} \phi_k^{z'} x\,\mathrm{d}A_f\right), \tag{62b}$$

$$C_{Q_k\eta_l\cos\bar{\alpha}} = \frac{4 l_{lb}}{M_\infty A_t}\left(\int_{A_{lb}} \phi_k^z \frac{\partial\phi_l^z}{\partial x}\,\mathrm{d}A_{lb} + 2\int_{A_f} \phi_k^{z'} \frac{\partial\phi_l^{z'}}{\partial x'}\,\mathrm{d}A_f\right), \tag{62c}$$

$$C_{Q_k\dot{\eta}_l} = -\frac{4}{M_\infty A_t}\left(\int_{A_{lb}} \phi_k^z\phi_l^z\,\mathrm{d}A_{lb} + 2\int_{A_f} \phi_k^{z'}\phi_l^{z'}\,\mathrm{d}A_f\right). \tag{62d}$$

3.5. Structural dynamic model based on equivalent plate approach

The configuration selected for the generic hypersonic vehicle resembles the X-33 RLV, as shown in Fig. 13. The initial structural model consists of isotropic equivalent plate segments and nonstructural masses for the canted fins, clipped delta-shaped main lifting body, fuel and payload. The mass and stiffness properties of the equivalent plate model are determined by matching the calculated mode shapes and frequencies to those obtained from a detailed NASTRAN model of the empty vehicle. This simple configuration was chosen to facilitate methodology development.

The solution of the governing equations of motion for the unrestrained vehicle requires the determination of the normal modes and frequencies of the unrestrained (or free–free) vehicle. The equivalent plate code, ELAPS, is used to model the vehicle and compute the unrestrained mode shapes. A concise description of the equivalent plate model is provided for completeness.

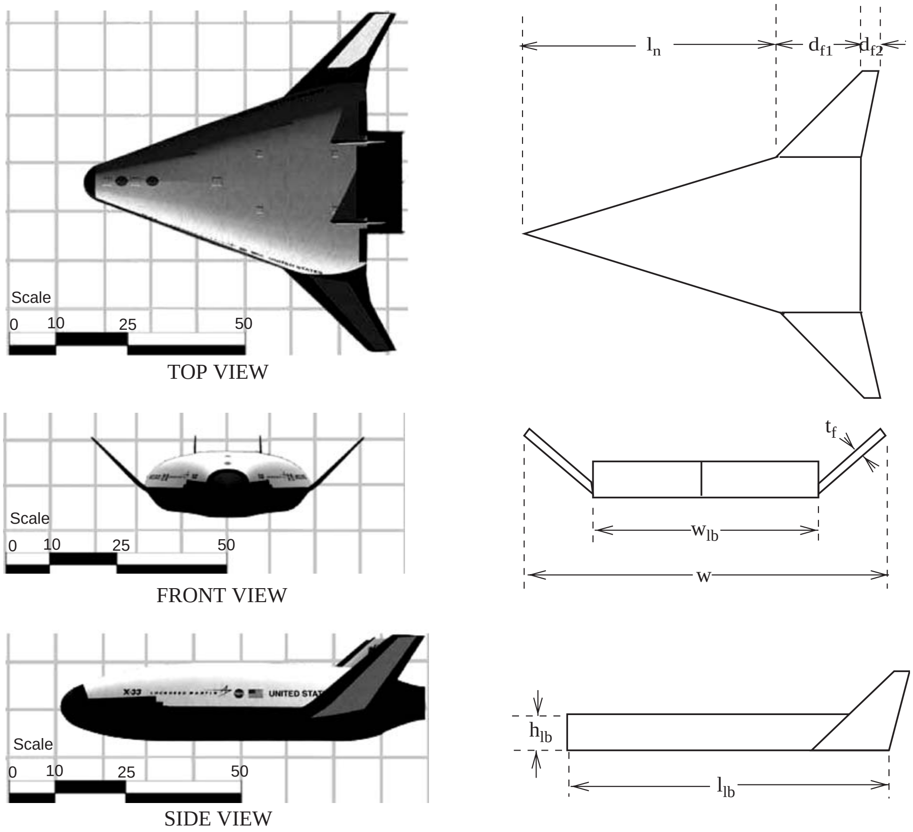

Fig. 13. Actual and idealized X-33 configurations.

In equivalent plate theory, the vehicle planform geometry is divided into multiple trapezoidal segments with cross-sectional geometry specified by the analyst in the form of polynomial series in the global coordinates, x and y:

$$\begin{aligned} Z_c(x,y) &= \sum_{i=0}^{m}\sum_{j=0}^{n} z_{ij}x^i y^j, \\ h^b(x,y) &= \sum_{i=0}^{m}\sum_{j=0}^{n} h^b_{ij}x^i y^j, \\ t_k(x,y) &= \sum_{i=0}^{m}\sum_{j=0}^{n} t_{ij}x^i y^j, \end{aligned} \tag{63}$$

where the physical description of the quantities used in Eq. (63) is shown in Fig. 14. The displacement field for the equivalent plate is assumed to be of the form

$$u_x = u_{x0} - z\frac{\partial u_{z0}}{\partial x} + z\Phi_x, \tag{64a}$$

$$u_y = u_{y0} - z\frac{\partial u_{z0}}{\partial y} + z\Phi_y, \tag{64b}$$

$$u_z = u_{z0}, \tag{64c}$$

where u_{x0}, u_{y0}, and u_{z0} are the middle surface displacements in the x, y, and z directions, respectively, and Φ_x, Φ_y are additional degrees of freedom that are necessary for transverse shear deformation modelling. The reference surface

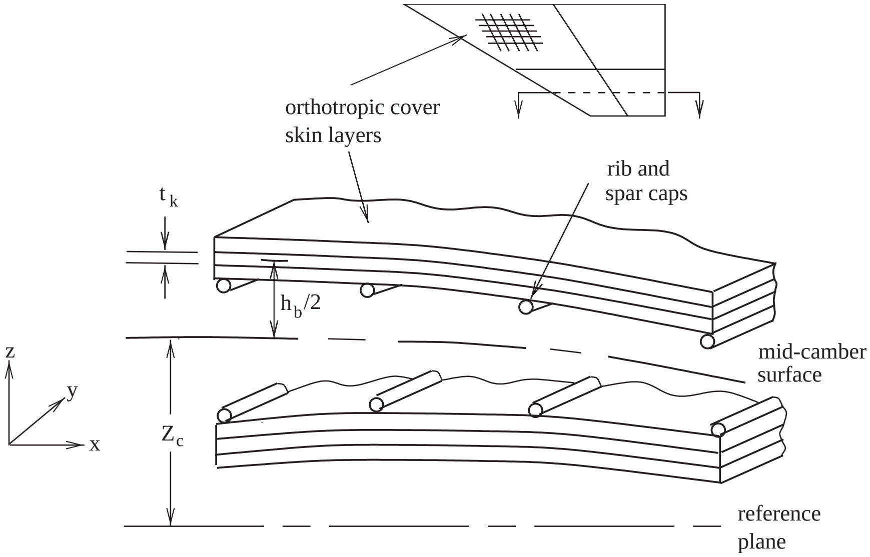

Fig. 14. Vehicle structural box used in equivalent plate modelling.

displacements and transverse shear rotations are approximated by polynomial displacement functions as

$$u_{x0} = \boldsymbol{\phi}_{\mathbf{x}}^{\mathrm{T}}\mathbf{q}_{\mathbf{x}}, \quad u_{y0} = \boldsymbol{\phi}_{\mathbf{y}}^{\mathrm{T}}\mathbf{q}_{y}, \ u_{z0} = \boldsymbol{\Phi}_{\mathbf{z}}^{\mathrm{T}}\mathbf{q}_{z}, \tag{65a}$$

$$\boldsymbol{\Phi}_{\mathbf{x}} = \boldsymbol{\Phi}_{\boldsymbol{\Phi}_{\mathbf{x}}}^{\mathrm{T}}\mathbf{q}_{\boldsymbol{\Phi}_{\mathbf{x}}}, \quad \boldsymbol{\Phi}_{y} = \boldsymbol{\phi}_{\boldsymbol{\Phi}_{\mathbf{y}}}^{\mathrm{T}}\mathbf{q}_{\boldsymbol{\Phi}_{\mathbf{y}}}, \tag{65b}$$

where $\phi_x, \mathbf{q}_x$ are (expressions for $\phi_y - \mathbf{q}_{\boldsymbol{\Phi}_y}$ are similar)

$$\boldsymbol{\phi}_{\mathbf{x}}^{\mathbf{T}} = [1, x, x^2, \ldots, y, xy, x^2y, \ldots, x^I y^J], \tag{66a}$$

$$\mathbf{q}_{\mathbf{x}}^{\mathbf{T}} = [q_{x_{00}}, q_{x_{10}}, q_{x_{20}}, \ldots, q_{x_{01}}, q_{x_{11}}, q_{x_{21}}, \ldots, q_{x_{IJ}}]. \tag{66b}$$

In Eq. (66b), $\mathbf{q}_{\mathbf{x}} - \mathbf{q}_{\Phi_y}$ are the unknown generalized coordinates, obtained from the solution of the global system of equations.

Out-of-plane sections, such as the canted fins on the X-33, are accommodated by defining an additional displacement system for the section and connecting the displacement systems with stiff springs to ensure displacement compatibility. Boundary conditions may be enforced either by using springs or by setting the appropriate coefficients in the assumed displacement function to zero. Taking advantage of symmetry, the vehicle shown in Fig. 13 is modelled in ELAPS by defining only the right half-plane, with boundary conditions enforced at the vehicle center-line.

The global mass and stiffness matrices are assembled from the contributions of each structural component, and the natural modes and frequencies of the unrestrained vehicle are then obtained by solving the linear eigenvalue problem. For a comprehensive discussion of equivalent plate theory and recent enhancements; see Giles (1989, 1995).

3.6. Stability boundary condition

The stability boundaries for the generic hypersonic vehicle are determined from the eigenproblem generated from the governing equations of motion. Therefore, the equations of motion, Eqs. (36) are rewritten in matrix form

$$D_{\hat{t}}\boldsymbol{\Delta}\mathbf{x} = \begin{bmatrix} \mathbf{A}_{\mathbf{r}} & \mathbf{A}_{\mathbf{rf}} & \mathbf{A}_{\mathbf{r}\dot{\mathbf{f}}} \\ \mathbf{O} & \mathbf{O} & \mathbf{I} \\ \mathbf{A}_{\dot{\mathbf{f}}\mathbf{r}} & \mathbf{A}_{\dot{\mathbf{f}}\,\mathbf{f}} & \mathbf{A}_{\dot{\mathbf{f}}\dot{\mathbf{f}}} \end{bmatrix} \boldsymbol{\Delta}\mathbf{x} = \mathbf{A}\boldsymbol{\Delta}\mathbf{x}, \tag{67}$$

where

$$\mathbf{\Delta x} = \left\{ \begin{array}{c} \Delta\alpha \\ \Delta\hat{q} \\ \Delta\hat{v}_1 \\ \vdots \\ \Delta\hat{v}_{2N_m} \end{array} \right\}, \tag{68}$$

and the submatrices of the partitioned matrix, A, are given in Appendix B. Solutions to Eqs. (67) can be written as

$$\mathbf{\Delta x} = \xi e^{\lambda\hat{t}}, \tag{69}$$

which produce the eigenvalue problem from which the aeroelastic stability boundaries are obtained

$$(\mathbf{A} - \lambda\mathbf{I})\boldsymbol{\xi} = 0. \tag{70}$$

Table 3
Natural frequencies (Hz) calculated from ELAPS

Mode no.	Empty	10% fuel	50% fuel	100% fuel
1	5.21	5.17	5.1	5.01
2	5.53	5.43	5.23	5.12
3	11.1	9.8	7.05	5.61
4	12.46	11.34	8.48	6.78
5	13.48	12.93	10.1	8.07
6	13.91	13.51	10.71	8.67

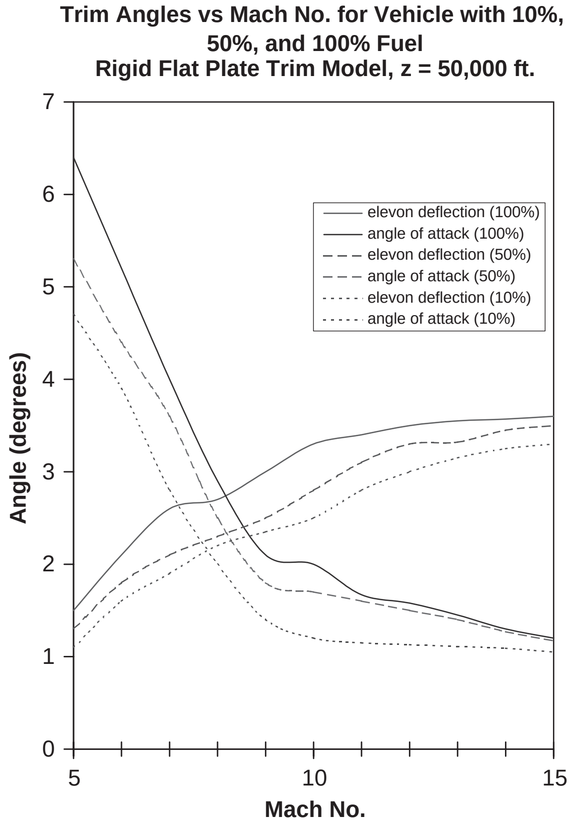

Fig. 15. Trim curves for fueled vehicle.

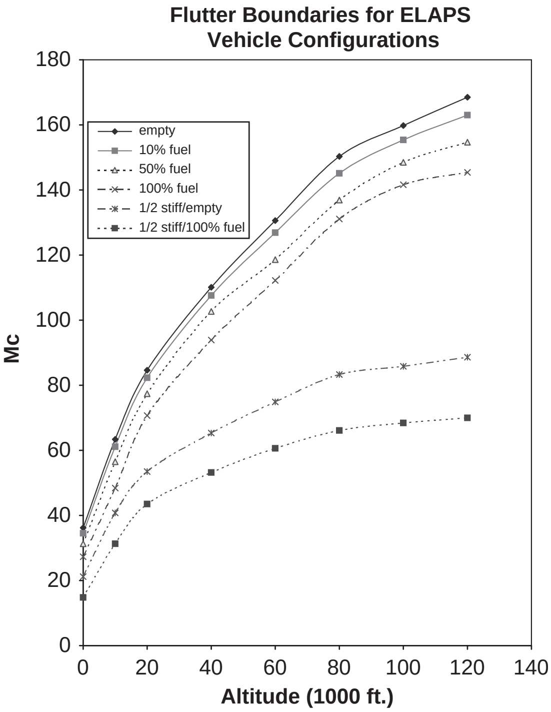

Fig. 16. Flutter boundaries for generic hypersonic vehicle.

The eigenvalues, $\lambda_n = \zeta_n + i\omega_n$, are calculated in an iterative manner. Starting at low values of the flight speed, V_{0x}, the eigenvalues are computed, and the process is repeated until the real part of any particular eigenvalue becomes zero. At each iteration, the trim state is calculated using the current value of V_{0x}. This process is repeated at a number of altitudes representing the operational envelope of the vehicle.

3.7. Results for complete hypersonic vehicle in trimmed flight

The baseline hypersonic vehicle configuration chosen for this study has the following properties. The vehicle has a length of 65 ft and a width of 65 ft (l_{lb} and w in Fig. 13, respectively). The vehicle is made of aluminum and has a structural weight of 73 000 lbs. Fuel weight at takeoff is 210 000 lbs. Four fuel configurations were studied: the empty vehicle, 10% fuel, 50% fuel and 100% fuel. Natural frequencies for each configuration were computed using ELAPS and are shown in Table 3. As mentioned, the model was tuned to approximately match the frequencies with those from a detailed NASTRAN model. These mode shapes are shown in (Nydick and Friedmann, 1999).

Typical trim curves for the generic hypersonic vehicle are given in Fig. 15 for the four different fuel configurations. The trim angles are quite small at large Mach numbers; this is due to the large aerodynamic forces at these flight conditions. Effect of the, c.g., location on the trim state was also considered (Nydick and Friedmann, 1999; Nydick, 2000). In these figures, x is the, c.g., location measured from the vehicle nose and is given as a fraction of total vehicle length. The angle of attack decreases as the, c.g., moves rearward but the elevon angle increases to large values due to the need to balance the increasing contribution to the moment from the main lifting body.

The flutter boundaries for the baseline vehicle configuration with four fuel conditions as well as a half-stiffness model with two fuel conditions are shown in Fig. 16. The flutter Mach number is very high for the altitudes at which the vehicle will fly in the hypersonic regime. For example, at 100 000 ft, Mc = 160 for the empty vehicle. The fully fueled vehicle is less stable, and flutter begins at around Mc = 140. If the stiffness is reduced by a factor of two, Mc decreases significantly. For the empty and fully fueled vehicles, it decreases to 86 and 68, respectively. The effect of, c.g., location on the flutter boundaries is shown in Fig. 17 for the half-stiffness 100% fuel configuration. Moving the, c.g., rearward initially reduces the stability but between $X_{cg} = 0.65$ and $X_{cg} = 0.7$ the stability begins to increase.

These results indicate that for the particular vehicle configuration selected, flutter at high speeds and high altitudes is not possible at the operational speed of the vehicle, mainly because the dynamic pressure is low at very high altitudes.

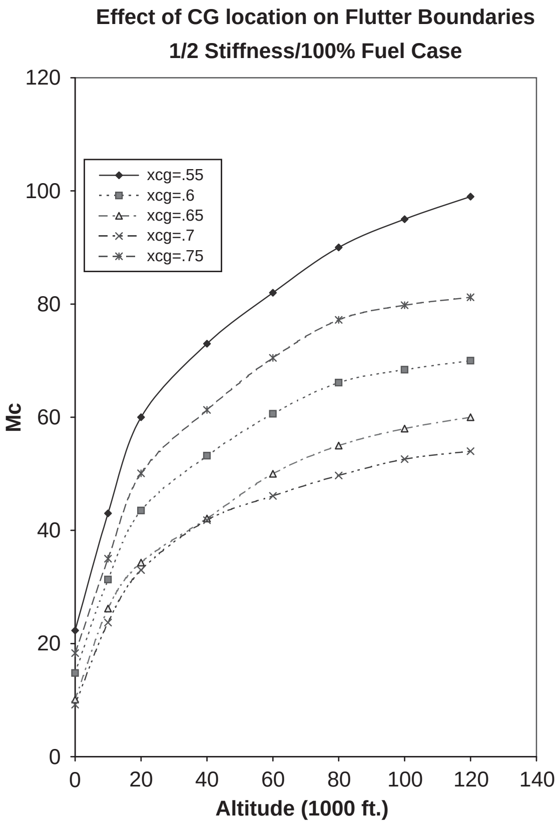

Fig. 17. Effect of vehicle, c.g., location on flutter boundaries.

4. Concluding remarks

This paper presents aeroelastic analyses for two configurations: (a) a typical cross-section representing a double-wedge airfoil in two-dimensional hypersonic flow and (b) a complete unrestrained generic hypersonic vehicle that resembles a reusable launch vehicle. For the first configuration, the unsteady airloads were determined from piston theory, the solution of the Euler and solution of the Navier–Stokes equations, and the primary objective is to assess the differences in aeroelastic stability due to the various airload models.

The second configuration models the global aeroelastic behavior of a generic unrestrained vehicle, and the airloads are based on linear piston theory. Based on the numerical results presented in the paper, the following conclusions can be stated.

1. For certain combinations of high Mach numbers and offsets between elastic axis and midchord there can be large differences between aeroelastic stability margins based on first- and third-order piston theory. Predictions of aeroelastic stability based on linear piston theory can be unreliable, and the boundaries are not conservative.
2. The aeroelastic behavior of the double-wedge typical section at subcritical Mach numbers exhibits fairly similar behavior when loads are generated from third-order piston theory, Euler or Navier–Stokes solutions. The frequency and damping characteristics are also comparable. The differences increase substantially at, and beyond, the stability boundary.
3. The stability boundaries predicted, for the double-wedge typical section, by Euler solutions are approximately 20–25% lower than those predicted by piston theory. The Navier–Stokes solutions are approximately 5% further below the Euler-based solutions.
4. The various aeroelastic models predict similar trends due to changes in parameters such as: offsets between elastic axis and midchord, wedge angle and static angle of attack for the double-wedge typical section.
5. For the entire vehicle, flutter margins can be sensitive to trim conditions and, c.g., location, which are determined to a large extent by the amount of fuel in the vehicle.

Acknowledgements

The authors thank Drs R. Bartels and R. Biedron from NASA Langley Research Center for the CFL3D code and for their help in using the code. This research was supported in part by AFOSR Grant F49620-01-0158 with Dr D. Mook as program manager.

Appendix A

The various nondimensional quantities required for the equations of motion are given below

$$\begin{aligned}
&\hat{m} = \frac{2m}{\rho_\infty A_t l_{lb}}, \quad \hat{J}^0_{yy} = \frac{2J^0_{yy}}{\rho_\infty A_t l^3_{lb}},\\
&\hat{t} = \frac{\bar{V}_{0x} t}{l_{lb}}, \quad D_{\hat{t}}() = \frac{\mathrm{d}}{\mathrm{d}\hat{t}}(),\\
&\hat{M}^g_k = \frac{2M^g_k}{\rho_\infty A_t l_{lb}}, \quad \hat{\omega}_k = \frac{\omega_k l_{lb}}{\hat{V}_{0x}},\\
&\Delta\alpha = \frac{\Delta v_{0z}}{V_{0x}}, \quad \Delta\hat{q} = \frac{l_{lb}\Delta q}{V_{0x}},\\
&\Delta\hat{\eta}_i = \frac{\Delta\eta_i}{l_{lb}}, \quad \Delta\hat{\eta}_{N_{m+i}} = \frac{\Delta\eta_{N_{m+i}}}{\hat{V}_{0x}}.
\end{aligned} \tag{A.1}$$

The flutter derivatives are defined next as follows:

$$Z_{v_{0z}} = \tfrac{1}{2}\rho_\infty \bar{V}_{0x} A_t C_{z\alpha}, \tag{A.2a}$$

$$Z_q = \tfrac{1}{2}\rho_\infty \bar{V}_{0x} A_t l_{lb} C_{zq}, \tag{A.2b}$$

$$Z_{\eta_i} = \frac{1}{2l_{lb}}\rho_\infty \bar{V}^2_{0x} A_t C_{z\eta_i}, \tag{A.2c}$$

$$Z_{\dot{\eta}_i} = \tfrac{1}{2}\rho_\infty \bar{V}_{0x} A_t C_{z\dot{\eta}_i}, \tag{A.2d}$$

$$Z_{\delta_e} = \tfrac{1}{2}\rho_\infty \bar{V}^2_{0x} A_t C_{z\delta_e}, \tag{A.2e}$$

$$M_{v_{0z}} = \tfrac{1}{2}\rho_\infty \bar{V}_{0x} A_t l_{lb} C_{m\alpha}, \tag{A.2f}$$

$$M_q = \tfrac{1}{2}\rho_\infty \bar{V}_{0x} A_t l^2_{lb} C_{mq}, \tag{A.2g}$$

$$M_{\eta_i} = \tfrac{1}{2}\rho_\infty \bar{V}^2_{0x} A_t C_{m\eta_i}, \tag{A.2h}$$

$$M_{\dot{\eta}_i} = \tfrac{1}{2}\rho_\infty \bar{V}^2_{0x} A_t C_{m\dot{\eta}_i}, \tag{A.2i}$$

$$M_{\delta_e} = \tfrac{1}{2}\rho_\infty \bar{V}^2_{0x} A_t l_{lb} C_{m\delta_e}, \tag{A.2j}$$

$$\hat{Q}_{kv_{0z}} = \tfrac{1}{2}\rho_\infty \bar{V}_{0x} A_t C_{Q_k\alpha}, \tag{A.2k}$$

$$\hat{Q}_{k_q} = \tfrac{1}{2}\rho_\infty \bar{V}_{0x} A_t l_{lb} C_{Q_k q}, \tag{A.2l}$$

$$\hat{Q}_{k_{\eta_l}} = \frac{1}{2l_{lb}}\rho_\infty \bar{V}^2_{0x} A_t C_{Q_k\eta_l}, \tag{A.2m}$$

$$\hat{Q}_{k_{\dot{\eta}_l}} = \tfrac{1}{2}\rho_\infty \bar{V}_{0x} A_t C_{Q_k\dot{\eta}_i}. \tag{A.2n}$$

Appendix B

$$\mathbf{A}_r = \begin{bmatrix} \dfrac{C_{z\alpha}}{\hat{m}} & 1+\dfrac{C_{zq}}{\hat{m}} \\ \dfrac{C_{m\alpha}}{\hat{J}_0^{yy}} & \dfrac{C_{m\alpha}}{\hat{J}_0^{yy}} \end{bmatrix}_{(2\times 2)}, \tag{B.1}$$

$$\mathbf{A}_{rf} = \begin{bmatrix} \dfrac{C_{z\eta 1}}{\hat{m}} & \cdots & \dfrac{C_{z\eta_{N_m}}}{\hat{m}} \\ \dfrac{C_{m\eta 1}}{\hat{J}_0^{yy}} & \cdots & \dfrac{C_{z\eta_{N_m}}}{\hat{J}_0^{yy}} \end{bmatrix}_{(2\times N_m)}, \tag{B.2}$$

$$\mathbf{A}_{r\dot{f}} = \begin{bmatrix} \dfrac{C_{z\dot{\eta}_1}}{\hat{m}} & \cdots & \dfrac{C_{z\dot{\eta}_{N_m}}}{\hat{m}} \\ \dfrac{C_{m\dot{\eta}_1}}{\hat{J}_0^{yy}} & \cdots & \dfrac{C_{z\dot{\eta}_{N_m}}}{\hat{J}_0^{yy}} \end{bmatrix}_{(2\times N_m)}, \tag{B.3}$$

$$\mathbf{A}_{\dot{f}r} = \begin{bmatrix} \dfrac{C_{Q_1\alpha}}{\hat{M}_1^g} & \dfrac{C_{Q_1 q}}{\hat{M}_1^g} \\ \vdots & \vdots \\ \dfrac{C_{Q_{N_m}\alpha}}{\hat{M}_{N_m}^g} & \dfrac{C_{Q_{N_m}q}}{\hat{M}_{N_m}^g} \end{bmatrix}_{(N_m\times 2)}, \tag{B.4}$$

$$\mathbf{A}_{\dot{f}f} = \begin{bmatrix} \dfrac{C_{Q_{1\eta 1}}}{M_1^g} - \hat{\omega}_1^2 & \dfrac{C_{Q_{1\eta 2}}}{\hat{M}_1^g} & \cdots & \dfrac{C_{Q_{1\eta N_m}}}{\hat{M}_1^g} \\ \dfrac{Q_{2\eta 1}}{\hat{M}_2^g} & \dfrac{Q_{2\eta 2}}{\hat{M}_2^g} - \hat{\omega}_2^2 & \cdots & \dfrac{C_{Q_{2\eta N_m}}}{\hat{M}_2^g} \\ \vdots & \vdots & \ddots & \vdots \\ \dfrac{C_{Q_{N_m}\eta 1}}{\hat{M}_{N_m}^g} & \dfrac{C_{Q_{N_m}\eta 2}}{\hat{M}_{N_m}^g} & \vdots & \dfrac{C_{Q_{N_m}\eta_{N_m}}}{\hat{M}_{N_m}^g} - \hat{\omega}_{N_m}^2 \end{bmatrix} (N_m \times N_m), \tag{B.5}$$

$$\mathbf{A}_{\dot{f}}\dot{f} = \begin{bmatrix} \dfrac{C_{Q_{1\dot{\eta}1}}}{M_1^g} - 2\xi_1\hat{\omega}_1^2 & \dfrac{C_{Q_{1\dot{\eta}2}}}{\hat{M}_1^g} & \cdots & \dfrac{C_{Q_{1\dot{\eta}N_m}}}{\hat{M}_1^g} \\ \dfrac{Q_{2\dot{\eta}1}}{\hat{M}_2^g} & \dfrac{Q_{2\dot{\eta}2}}{\hat{M}_2^g} - 2\xi_2\hat{\omega}_2^2 & \cdots & \dfrac{C_{Q_{2\dot{\eta}N_m}}}{\hat{M}_2^g} \\ \vdots & \vdots & \ddots & \vdots \\ \dfrac{C_{Q_{N_m}\dot{\eta}1}}{\hat{M}_{N_m}^g} & \dfrac{C_{Q_{N_m}\dot{\eta}2}}{\hat{M}_{N_m}^g} & \vdots & \dfrac{C_{Q_{N_m}\dot{\eta}_{N_m}}}{\hat{M}_{N_m}^g} - 2\xi_{n_m}\hat{\omega}_{N_m}^2 \end{bmatrix} (N_m \times N_m). \tag{B.6}$$

References

Abbas, J.F., Ibrahim, R.A., 1993. Nonlinear flutter of orthotropic composite panel under aerodynamic heating. AIAA Journal 31 (8), 1478–1488.

Ashley, H., Zartarian, G., 1956. Piston theory—a new aerodynamic tool for the aeroelastician. Journal of the Aeronautical Sciences 23 (12), 1109–1118.

Bein, T., Friedmann, P.P., Zhong, X., Nydick, I., 1993. Hypersonic flutter of a curved shallow panel with aerodynamic heating. In: Proceedings of the 34th AIAA/ASME/ASCE/AHS/ASC Structures, Structural Dynamics and Materials Conference. No. AIAA Paper No. 93-1318, La Jolla, CA, USA.

Berry, S.A., Horvath, T.J., Hollis, B.R., Thompson, R.A., Hamilton, H.H., 1999. X-33 hypersonic boundary layer transition. In: 33rd AIAA Thermophysics Conference. No. AIAA Paper No. 99-3560, Norfolk, VA, USA.

Bilimoria, D.D., Schmidt, D.K., 1995. Integrated development of the equations of motion for elastic hypersonic flight vehicles. Journal of Guidance, Control, and Dynamics 18 (1), 73–81.

Bisplinghoff, R.L., Dugundji, J., 1958. In: Hoff, N.J. (Ed.), Influence of Aerodynamic Heating on Aeroelastic Phenomena in High Temperature Effects in Aircraft Structures, Agardograph No. 28. Pergamon Press, Oxford, pp. 288–312.

Bisplinghoff, R.L., Ashley, H., Halfman, R.L., 1955. Aeroelasticity. Addison-Wesley, Reading, MA.

Blades, E., Ruth, M., Fuhrman, D., 1999. Aeroelastic analysis of the x-34 launch vehicle. In: Proceedings of the 40th AIAA/ASME/ASCE/AHS/ASC Structures, Structural Dynamics and Materials Conference. No. AIAA Paper No. 99-1352, St. Louis, MO, USA, pp. 1321–1331.

Bousman, W.G., Winkler, D.J., 1981. Application of the moving-block analysis. In: Proceedings of the AIAA Dynamics Specialist Conference. No. AIAA 81-0653, Atlanta, GA, USA, pp. 755–763.

Cunningham, H.J.B., Bennett, R.M., 1989. Modern wing flutter analysis by computational fluid dynamic methods. Journal of Aircraft 25 (10), 962–968.

Garrick, I.E., 1963. A survey of aerothermoelasticity. Aerospace Engineering 22 (1), 140–147.

Giles, G.L., 1986. Equivalent plate analysis of aircraft wing-box structures with general planform geometry. Journal of Aircraft 23 (11), 859–864.

Giles, G.L., 1989. Further generalization of an equivalent plate representation for aircraft structural analysis. Journal of Aircraft 26 (1), 67–74.

Giles, G.L., 1995. Equivalent plate modelling for conceptual design of aircraft wing structures. In: Proceedings of the First AIAA Aircraft Engineering, Technology and Operations Congress. No. AIAA Paper No. 95-3945, Los Angeles, CA, USA.

Gray, E.G., Mei, C., 1992. Large-amplitude finite element flutter analysis of composite panels in hypersonic flow. In: Proceedings of the 33rd AIAA/ASME/ASCE/AHS/ASC Structures, Structural Dynamics and Materials Conference. No. AIAA Paper No. 90-0982, Dallas, TX, USA, pp. 492–512.

Gupta, K.K., Voelker, L.S., Bach, C., Doyle, T., Hahn, E., 2001. Cfd-based aeroelastic analysis of the x-43 hypersonic flight vehicle. In: 39th Aerospace Sciences Meeting and Exhibit. No. AIAA Paper No. 2001-0712.

Hedgepeth, I.E., Widmayer, E., 1963. Dynamic and aeroelastic problems of lifting re-entry bodies Aerospace Engineering 22 (1), 148–153.

Heeg, J., Gilbert, M.G., 1993. Active control of aerothermoelastic effects for a conceptual hypersonic aircraft. Journal of Aircraft 30, 453–458.

Heeg, J., Zeiler, T.A., Pototzky, A., Spain, C., Engelund, W., 1993. Aerothermoelastic analysis of a nasp demonstrator model. In: Proceedings of the 34th AIAA/ASME/ASCE/AHS/ASC Structures, Structural Dynamics and Materials Conference. No. AIAA Paper No. 93-1366, La Jolla, CA, pp. 617–627.

Krist, S.L.B., Rumsey, C.L., 1997. Cfl3d User's Manual (version 5.0), NASA Langley Research Center, VA, USA.

Laidlaw, W.R., Wyker, J.H., 1963. Potential aerothermoelastic problems associated with advanced vehicle design Aerospace Engineering 22(1), 154–164

Lees, L., 1955. Hypersonic flow. In: Fifth International Aeronautical Conference, Los Angeles, CA, pp. 241–276.

Lighthill, M.J., 1953. Oscillating airfoils at high mach numbers. Journal of the Aeronautical Sciences 20 (6), 402–406.

Livne, E., 1993. Recent developments in equivalent plate modelling for wing shape optimization. In: Proceedings of the 34th AIAA/ASME/ASCE/AHS/ASC Structures, Structural Dynamics and Materials Conference. No. AIAA Paper No. 93-1647, La Jolla, CA, USA, pp. 2998–3011.

Mei, C., Abdel-Motagly, K., Chen, K., 1999. Review of nonlinear panel flutter at supersonic and hypersonic speeds. Applied Mechanics Reviews 52 (10), 321–332.

Meirovitch, L., 1991. Hybrid state equations of motion for flexible bodies in terms of quasi-coordinates. Journal of Guidance, Control, and Dynamics 14 (5), 1008–1013.

Milne, R.D., 1955. Dynamics of the deformable aeroplane, parts i and ii. Technical Report R & M No. 3345, Great Britain Aeronautical Research Council.

Milne, R.D., 1968. Some remarks on the dynamics of deformable bodies. AIAA Journal 6, 556.

Nydick, I., 2000. Studies in hypersonic aeroelasticity. Ph.D. Thesis, University of California, Los Angeles, USA.

Nydick, I., Friedmann, P.P., 1999. Aeroelastic analysis of a generic hypersonic vehicle. In: Proceedings of the CEAS/AIAA/ICASE/NASA Langley International Forum on Aeroelasticity and Structural Dynamics. No. NASA/CP-1999-209136/PT2, Williamsburg, VA, USA, pp. 777–810.

Nydick, I., Friedmann, P.P., Zhong, X., April 1995. Hypersonic panel flutter studies on curved panels. In: Proceedings of the 36th AIAA/ASME/ASCE/AHS/ASC Structures, Structural Dynamics and Materials Conference. No. AIAA Paper No. 95-1485, New Orleans, LA, pp. 2995–3011.

Rasmussen, M., 1994. Hypersonic Flow. Wiley, New York.

Ricketts, R., Noll, T., Whitlow, W., Huttsell, L., 1993. An overview of aeroelasticity studies for the national aerospace plane. In: Proceedings of the 34th AIAA/ASME/ASCE/AHS/ASC Structures, Structural Dynamics and Materials Conference. No. AIAA Paper No. 93-1313, La Jolla, CA, USA, pp. 152–162.

Riley, C.J.K., Alter, S.J., 1998. Aeroheating predictions for x-34 using an inviscid-boundary layer method. In: 36th Aerospace Sciences Meeting and Exhibit. No. AIAA 98-0880, Reno, NV, USA.

Robinson, B.A.B., Yang, H.T., 1991. Aeroelastic analysis of wings using the Euler equations with a deforming mesh. Journal of Aircraft 28, 778–788.

Rodgers, J.P., 1992. Aerothermoelastic analysis of a nasp-like vertical fin. In: Proceedings of the 33rd AIAA/ASME/ASCE/AHS Structures, Structural Dynamics and Materials Conference. No. AIAA-92-2400-CP, Dallas, TX, USA.

Scott, R.C., Pototzky, A.S., 1993. A method of predicting quasi-steady aerodynamics for flutter analysis of high speed vehicles using steady cfd calculations. In: Proceedings of the 34th AIAA/ASME/ASCE/AHS/ASC Structures, Structural Dynamics and Materials Conference. No. AIAA Paper No. 93-1364, La Jolla, CA, USA, pp. 595–603.

Spain, C., Zeiler, T.A., Gibbons, M.D., Soistmann, D.L., Pozefsky, P., DeJesus, R.O., Brannon, C.P., 1993a. Aeroelastic character of a national aerospace plane demonstrator concept. In: Proceedings of the 34th AIAA/ASME/ASCE/AHS/ASC Structures, Structural Dynamics and Materials Conference. No. AIAA Paper No. 93-1314, La Jolla, CA, USA, pp. 163–170.

Spain, C., Zeiler, T.A., Gibbons, M.D., Soistmann, D.L., Pozefsky, P., DeJesus, R.O., Brannon, C.P., 1993b. Aeroelastic character of a national aerospace plane demonstrator concept. In: Proceedings of the 34th AIAA/ASME/ASCE/AHS/ASC Structures, Structural Dynamics and Materials Conference, La Jolla, CA, USA, pp. 163–170.

Thuruthimattam, B.J., Friedmann, P.P., McNamara, J.J., Powell, K.G., 2002. Aeroelasticity of a generic hypersonic vehicle. In: Proceedings of the 43rd AIAA/ASME/ASCE/AHS Structures, Structural Dynamics and Materials Conference. No. AIAA Paper No. 2002-1209, Denver, CO, USA.

Waszak, M.R., Schmidt, D.K., 1988. Flight dynamics of aeroelastic vehicles. Journal of Aircraft 23 (6), 562–571.

Xue, D.Y., Mei, C., 1990. Finite element two-dimensional panel flutter at high supersonic speeds and elevated temperature. In: Proceedings of the 31st AIAA/ASME/ASCE/AHS/ASC Structures, Structural Dynamics and Materials Conference. No. AIAA Paper No. 90-0982, Long Beach, CA, USA, pp. 1464– 1475.